

## **PAPER • OPEN ACCESS**

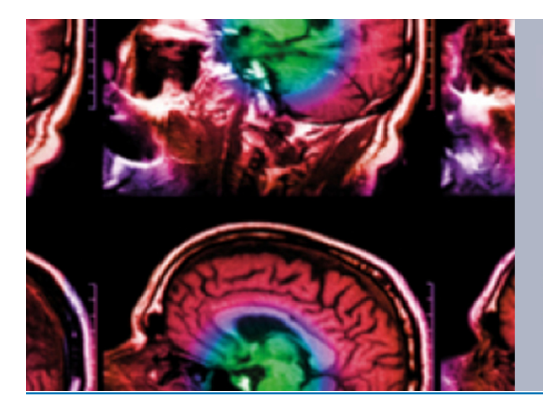
# Monte Carlo investigation of electron fluence perturbation in MRI-guided radiotherapy beams using six commercial radiation detectors

To cite this article: Yunuen Cervantes et al 2022 Phys. Med. Biol. 67 035001

View the article online for updates and enhancements.

# You may also like

- Electron fluence perturbation correction factors for solid state detectors irradiated in megavoltage electron beams Paul N Mobit, George A Sandison and Alan E Nahum
- Breakdown of Bragg—Gray behaviour for low-density detectors under electronic disequilibrium conditions in small megavoltage photon fields
  Sudhir Kumar, John D Fenwick, Tracy S A Underwood et al.
- Monte-Carlo-computed dose, kerma and fluence distributions in heterogeneous slab geometries irradiated by small megavoltage photon fields
   Sudhir Kumar, Alan E Nahum and Indrin J Chetty



# IPEM IOP

Series in Physics and Engineering in Medicine and Biology

Your publishing choice in medical physics, biomedical engineering and related subjects.

Start exploring the collection-download the first chapter of every title for free.

# Physics in Medicine & Biology



#### **OPEN ACCESS**



# 17 August 2021

#### REVISED

10 December 2021

#### ACCEPTED FOR PUBLICATION

13 January 2022

#### PUBLISHED

27 January 2022

Original content from this work may be used under the terms of the Creative

Any further distribution of this work must maintain attribution to the author(s) and the title of the work, journal citation



#### **PAPER**

# Monte Carlo investigation of electron fluence perturbation in MRIguided radiotherapy beams using six commercial radiation detectors

Yunuen Cervantes<sup>1,2,\*</sup>, Simon Duane<sup>3</sup> and Hugo Bouchard<sup>1,2,4</sup>

- Département de physique, Université de Montréal, Complexe des sciences, 1375 Avenue Thérèse-Lavoie-Roux, Montréal, Québec H2V
- Centre de recherche du Centre hospitalier de l'Université de Montréal, 900 Rue Saint-Denis, Montréal, Québec, H2X 0A9, Canada
- National Physical Laboratory, Chemical, Medical and Environmental Science Department, Teddington, United Kingdom
- Département de radio-oncologie, Centre hospitalier de l'Université de Montréal (CHUM), 900 Rue Saint-Denis, Montréal, Québec, H2X 0A9, Canada
- Author to whom any correspondence should be addressed.

E-mail: yunuen.cervantes-espinosa@crchudequebec.ulaval.ca

Keywords: magnetic fields, reference dosimetry, ionization chamber, solid-state detectors, electron fluence, small fields, Monte Carlo

#### Abstract

With the integration of treatments with MRI-linacs to the clinical workflow, the understanding and characterization of detector response in reference dosimetry in magnetic fields are required. The external magnetic field perturbs the electron fluence. The degree of perturbation depends on the irradiation conditions and on the detector type. The purpose of this study is to evaluate the magnetic field impact on the electron fluence spectra in several detectors to provide a deeper understanding of detector response in these conditions. Monte Carlo calculations of the electron fluence are performed in six detectors (solid-state: PTW60012 and PTW60019, ionization chambers: PTW30013, PTW31010, PTW31021, and PTW31022) in water and irradiated by a 7 MV FFF photon beam with a small and a reference field, at 0 and 1.5 T. Three chamber axis orientations are investigated: parallel or perpendicular (either the Lorentz force pointing towards the stem or the tip) to the magnetic field and always perpendicular to the photon beam. One orientation for the solid-state detector is studied: parallel to the photon beam and perpendicular to the magnetic field. Additionally, electron fluence spectra are calculated in modified detector geometries to identify the underlying physical mechanisms behind the fluence perturbations. The total electron fluence in the Farmer chamber varies up to 1.24% and 5.12% at 1.5 T, in the parallel and perpendicular orientation, respectively. The interplay between the gyration radius and the Farmer chamber cavity length significantly affects the electron fluence in the perpendicular orientation. For the smallcavity chambers, the maximal variation in total electron fluence is 0.19% in the parallel orientation for the reference field. Significant small-field effects occur in these chambers; the magnetic field reduces the total electron fluence (with respect to the no field case) between 9.86% and 14.50%, depending on the orientation. The magnetic field strongly impacted the solid-state detectors in both field sizes, probably due to the high-Z components and cavity density. The maximal reductions of total electron fluence are 15.06  $\pm$  0.09% (silicon) and 16.00  $\pm$  0.07% (microDiamond). This work provides insights into detector response in magnetic fields by illustrating the interplay between several factors causing dosimetric perturbation effects: (1) chamber and magnetic field orientation, (2) cavity size and shape, (3) extracameral components, (4) air gaps and their asymmetry, (5) electron energy. Low-energy electron trajectories are more susceptible to change in magnetic fields, and are associated with detector response perturbation. Detectors with higher density and high-Z extracameral components exhibit more significant perturbations in the presence of a magnetic field, regardless of field size.

#### 1. Introduction

With the integration of magnetic resonance imaging with clinical linear accelerators (MRI-linacs), the characterization of different types of detectors for reference dosimetry measurements in MRI-linacs has been under investigation (Meijsing et al 2009, Reynolds et al 2013, O'Brien et al 2016, Wolthaus et al 2016, Malkov and Rogers 2017, Spindeldreier et al 2017, de Prez et al 2019, Pojtinger et al 2019, Billas et al 2020, Cervantes et al 2020). The majority of these studies focus on the characterization of ionization chamber responses and the calculation of correction factors in the presence of magnetic fields, either by experimental measurements, Monte Carlo calculations or both. Detector response depends on the detector geometry, magnetic field strength and orientation, beam quality, field size, and the potential presence of air gaps around the chamber (de Pooter et al 2020). Nevertheless, the behaviour of detector response in the presence of a strong magnetic field is still not fully understood and remains a question of interest.

The presence of any detector perturbs the particle fluence at the point of measurement compared to that in the absence of the detector. The degree of the perturbation depends on the detector design and materials and on the irradiation conditions, i.e. magnetic field strength and direction, beam quality, and field size. Particle fluence perturbations are more pronounced for detectors with materials differing drastically from water in terms of atomic composition and density. For small field dosimetry, when the field size is comparable to the detector size, the particle fluence perturbations increase, mainly due to volume averaging perturbations, and in the case of ionization chambers, also due to density perturbations (Scott *et al* 2012).

The underlying physics behind the magnetic field effect on detector response, along with the effect of the irradiation field size, were investigated in previous work (Cervantes *et al* 2021). Perturbations coming from extracameral components (stem, cavity wall, central electrode), atomic composition, density and volume of the detector were studied. The results showed that for small-cavity ionization chambers, the impact of the magnetic field was stronger in the density perturbation factor irradiated by fields smaller than  $1 \times 1$  cm<sup>2</sup>. On the contrary, for solid-state detectors (silicon diode and microDiamond detector), the magnetic field strongly increases the perturbations from extracameral components in fields larger than  $1 \times 1$  cm<sup>2</sup>. Even though this work provided an overview of dose perturbation factors, the interplay between cavity geometry, density and magnetic field was not fully described.

The objectives of this work are to detail the following effects due to the presence of a magnetic field: (1) fluence perturbations enhanced by high-Z components and cavity density, (2) the sensitivity of low energy electrons to fluence perturbations, (3) various geometrical effects related to cavity dimensions and orientation with respect to electron energy and field strength, and (4) fluence perturbations due to the presence air gaps of different shapes. Firstly, to demonstrate the first objective, the theoretical basis demonstrating the link between electron fluence perturbations and low-energy electrons with small gyration radii is presented in section 2.1, along with restrictions of Fano's theorem in the presence of magnetic fields. Secondly, to provide insights into the drastic effects of density and high-Z components, the variations in electron spectral fluence in six different detectors (one Farmer ionization chamber, three small-cavity chambers and two solid-state detectors) are characterized in narrow and broad beams coupled to magnetic fields, using different configurations. Thirdly to describe the impact of detector geometry on electron fluence in the presence of magnetic fields, in section 3.4, a simple detector model is presented where the variation of electron pathlength due to the magnetic field explains the shape of the electron fluence spectra. Finally, the electron fluence perturbations due to symmetrical and asymmetrical air gaps surrounding different ionization chambers are evaluated.

# 2. Materials and methods

#### 2.1. Theory

This section demonstrates that density fluctuations and small curvature radii have significant anticipated effects on fluence perturbations. Additionally, a particular condition applicable to the external beam setup is proposed to fulfil the special conditions to validate the Fano theorem in the presence of magnetic fields (Bouchard and Bielajew 2015) and perform special Fano cavity test in the Monte Carlo simulations of radiation transport.

## 2.1.1. Definitions

Considering the following variables in the laboratory frame:

- r: the vector corresponding to the particle position in space
- p: the vector corresponding to the particle momentum
- $\hat{u}$ : the unit vector in the direction of the particle momentum

- $\beta$ : speed in units of c
- $\Sigma$ : mass macroscopic cross-section (in cm<sup>2</sup> g<sup>-1</sup>)
- $f_i(\mathbf{r}, \mathbf{p})$ : the particle type i fluence differential in energy and direction corresponding to the number particles at r with momentum p per unit energy, per unit area perpendicular to  $\hat{u}$  and per unit solid angle  $d\hat{u} = \sin\theta d\theta d\phi$
- $F_i(\mathbf{r}, p)$ : the spectral distribution of a given  $f_i(\mathbf{r}, p)$  integrated over all directions, defined as

$$F_i(\mathbf{r}, p) \equiv \int_{4\pi} f_i(\mathbf{r}, \mathbf{p}) d\Omega. \tag{1}$$

• The spherical coordinates convention for representing  $\mathbf{p} = p\hat{\mathbf{u}}$  are

$$\hat{\boldsymbol{u}} = \sin \theta \cos \phi \hat{\boldsymbol{x}} + \sin \theta \sin \phi \hat{\boldsymbol{y}} + \cos \theta \hat{\boldsymbol{z}}$$

$$\hat{\boldsymbol{\theta}} = \cos \theta \cos \phi \hat{\boldsymbol{x}} + \cos \theta \sin \phi \hat{\boldsymbol{y}} - \sin \theta \hat{\boldsymbol{z}}$$

$$\hat{\boldsymbol{\phi}} = -\sin \phi \hat{\boldsymbol{x}} + \cos \phi \hat{\boldsymbol{y}}$$

$$\nabla_p = \hat{\boldsymbol{u}} \frac{\partial}{\partial p} + \hat{\boldsymbol{\theta}} \frac{1}{p} \frac{\partial}{\partial \theta} + \hat{\boldsymbol{\phi}} \frac{1}{p \sin \theta} \frac{\partial}{\partial \phi}$$

$$d\hat{\boldsymbol{u}} = d\cos \theta d\phi$$

- $S \equiv S(r, p)$ : the primary source term representing the number of particles of momentum p generated at r by an external source per unit mass, energy and direction (in  $g^{-1}$  MeV<sup>-1</sup> sr<sup>-1</sup>).
- $\mathcal{I}\{f; r\}$ : the interaction term is an operator representing the production of secondary particles (in  $g^{-1}$  MeV<sup>-1</sup>
- R: the gyration radius of charged particles subjected to a magnetic field of strength B.

#### 2.1.2. Radiation transport equation in the presence of magnetic fields

The Boltzmann radiation transport equation predicts the charged particle fluence rate by balancing the number of particles entering, created in and leaving the point of interest. It has been adapted to account for the presence of external electromagnetic fields by adding a term describing the effect of the Lorentz force on particle fluence in references (Bouchard and Bielajew 2015, Bouchard et al 2015). Considering the case free of an electric field, the radiation transport equation for charged particle fluence in the presence of an external magnetic field, B is

$$\hat{\boldsymbol{u}} \cdot \nabla_{\!r} f = \rho[S + \mathcal{I}\{f; \boldsymbol{r}\}] - q \,\hat{\boldsymbol{u}} \times \boldsymbol{B} \cdot \nabla_{\!r} f. \tag{2}$$

For choice of coordinates such that  $\mathbf{B} = B\hat{\mathbf{z}}$ , and using the equation (A2) derived in the appendix A for the Lorentz force term, then the transport equation becomes

$$\hat{\boldsymbol{u}} \cdot \nabla_{r} f = \rho \left[ S + \mathcal{I} \{ f; \, \boldsymbol{r} \} - \frac{1}{R\rho} \frac{\partial f}{\partial \phi} \right]. \tag{3}$$

Note that the energy-dependent gyration radius and the mass density are in the denominator of the last term on the right-hand side of the equation. Therefore, the impact of the magnetic field on electron fluence are expected to increase with small gyration radius and low-density materials. The electron gyration radius increases with increasing kinetic energy and decreasing magnetic field strength. Hence, in a constant magnetic field, lowenergy electrons have small gyration radii.

#### 2.1.3. Special Fano conditions

Under classical Fano conditions (Fano 1954), the following is fulfilled: (1) the atomic properties of the medium are homogeneous, hence  $\mathcal{I}\{f; r\} = \mathcal{I}\{f\}$ , and (2) the source produces equilibrium, i.e.  $S_{eq}$  is such that  $\nabla S_{\rm eq} = \mathbf{0}$ . Then, equation (3) becomes

$$\hat{\boldsymbol{u}} \cdot \nabla_{r} f = \rho \left[ S_{\text{eq}} + \mathcal{I} \{ f \} - \frac{1}{R\rho} \frac{\partial f}{\partial \phi} \right],$$

$$0 = S_{\text{eq}} + \mathcal{I} \{ f \} - \frac{1}{R\rho} \frac{\partial f}{\partial \phi},$$
(4)

and since the density is present in the last term, the secondary fluence is no longer independent of the density in the presence of an external electromagnetic field, hence Fano's theorem is no longer valid (Bouchard and

Bielajew 2015). Bouchard *et al* (2015) and De Pooter *et al* (2015) identified two special conditions to obtain equilibrium in this case. Fano's theorem is applicable in magnetic fields with the fulfilment of one of the following conditions:

The magnetic field strength is proportional to the mass density spatial distribution, such that  $\nabla(R\rho) = \mathbf{0}$ .

The source is isotropic, i.e.  $\frac{\partial S_{\text{eq}}}{\partial \theta} = \frac{\partial S_{\text{eq}}}{\partial \phi} = 0$ , which causes  $f_{\text{eq}}$  to be also isotropic, hence  $q(\hat{\boldsymbol{u}} \times \boldsymbol{B}) \cdot \nabla_{p} f_{\text{eq}} = 0$ .

Since condition 1 imposes a restriction on the magnetic field and not on the source (as condition 2 does), then it is more representative of an external beam geometry. Thus, the transport equation is

$$\hat{\boldsymbol{u}} \cdot \nabla_{r} f_{eq} = \rho \left[ S_{eq} + \mathcal{I} \{ f_{eq} \} - \frac{1}{R_{eq}} \frac{\partial f_{eq}}{\partial \phi} \right],$$

$$0 = S_{eq} + \mathcal{I} \{ f_{eq} \} - \frac{1}{R_{eq}} \frac{\partial f_{eq}}{\partial \phi},$$
(5)

with  $R_{\rm eq}=R\rho=\frac{p}{qB}$ . To fulfil the magnetic field proportionality to mass density in condition 1, the calculations of particle fluence can be performed in water, then the solution corresponds to the CPE spectrum prescribed by Fano's conditions, which is the same as in the absence of a magnetic field.

#### 2.1.4. Electron fluence spectra

To benchmark the electron fluence spectra calculations in the presence of magnetic fields, in this section, it is shown that the electron fluence spectrum is the same in the absence and presence of magnetic fields when the first special Fano condition is fulfilled. For this, the transport equation (5) is integrated over all directions

$$0 = \int_{4\pi} S_{\text{eq}} d\Omega + \int_{4\pi} \mathcal{I}\{f_{\text{eq}}\} d\Omega - \int_{4\pi} \frac{1}{R_{\text{eq}}} \frac{\partial f_{\text{eq}}}{\partial \phi} d\Omega, \tag{6}$$

defining a spectral source  $S_Q$  as

$$S_Q \equiv \int_{A^-} s_Q(\mathbf{r}, \mathbf{p}) d\Omega, \tag{7}$$

and the integration of the interaction term given by

$$\int_{4\pi} \mathcal{I}\{f(\mathbf{r}, \mathbf{p})\} d\Omega = -\Sigma(\mathbf{p})F(\mathbf{x}, \mathbf{p}) + \int_{\mathbf{p}}^{\infty} \Sigma(\mathbf{p}' \to \mathbf{p})F(\mathbf{x}, \mathbf{p}') d\mathbf{p}'$$

$$\equiv I\{F(\mathbf{r}, \mathbf{p})\},$$
(8)

with F the spectral distribution of f, defined in equation (1). The complete integration of the interaction term is presented in appendix B. Finally, the last term to integrate is

$$\int_{4\pi} \frac{1}{R_B \rho} \frac{\partial f}{\partial \phi} d\Omega = \frac{1}{R_B \rho} \int_0^{\pi} \sin\theta d\theta \int_0^{2\pi} \frac{\partial f}{\partial \phi} d\phi = 0.$$
 (9)

Then, the direction-integrated transport equation is

$$0 = S_O + I\{F(r, p)\}. \tag{10}$$

The solution to this equation is independent of magnetic fields. Hence, the electron fluence spectrum is the same in the absence and presence of magnetic fields when the first special Fano condition is fulfilled.

#### 2.2. Monte Carlo calculations

2.2.1. Validation of Monte Carlo calculations of electron fluence spectra in the presence of magnetic fields As shown in the theory (section 2.1.4), under the first special Fano condition, the Monte Carlo calculations of electron spectra in magnetic fields can be benchmarked with calculations in the absence of magnetic fields. Furthermore, an additional comparison can be made with the analytical approximation of the electron fluence spectra established by Kawrakow (2000). For this, the electron fluence is scored in a water voxel of 1 mm<sup>3</sup> at 10 cm depth inside a  $30 \times 30 \times 30$  cm<sup>3</sup> water phantom irradiated by a monoenergetic 1.25 MeV beam at 0 and 1.5 T, using the user code cavity from EGSnrc (Kawrakow *et al* 2017).

#### 2.2.2. Electron fluence in detectors

Monte Carlo calculations of the electron fluence differential in energy (or electron fluence, as it is referred to throughout the article) in six detectors are performed in the user code cavity from EGSnrc (Kawrakow *et al* 2017). In this code, the electron fluence differential in energy is normalized by the total incident photon fluence,

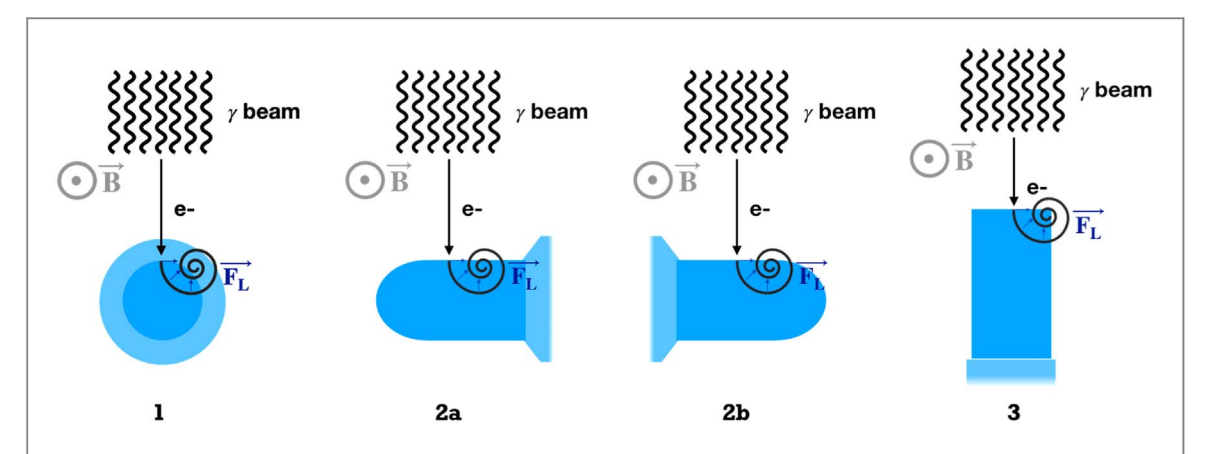


Figure 1. Diagram of three orientations for ionization chambers and one orientation for the solid-state detectors. (1) The chamber axis is parallel to the magnetic field, (2a) the chamber axis is perpendicular to the magnetic field and the Lorentz force ( $F_L$ ) points towards the stem, (2b) the chamber axis is perpendicular to the magnetic field with  $F_L$  pointing towards the tip and (3) the solid-state detector axis is perpendicular to the magnetic field and parallel to the beam.

Table 1. Detector specifications, taken from the manufacturer catalogue.

	PTW60012	PTW60019	PTW31022	PTW31021	PTW31010	PTW30013
Type of detector	Silicon diode	microDiamond	Pinpoint 3D	Semiflex 3D	Semiflex	Farmer
Sensitive volume diameter [mm]	1.0	2.2	2.9	4.8	5.5	6.1
Sensitive volume length [mm]	0.03	0.001	2.9	4.8	6.5	23.0
Nominal sensitive volume [mm <sup>3</sup> ]	0.25	0.004	16	70	125	600

 $F_0^{\rm tot}$ . The six detectors studied are a Farmer-type ionization chamber PTW30013 (PTW, Freiburg, Germany), three small-cavity ionization chamber models PTW31010, PTW31021, and PTW31022, the unshielded silicon diode PTW60012, and the microDiamond detector PTW60019. Detector size specifications are listed in table 1. The ionization chamber's active sensitive volumes were previously defined in Cervantes et~al~(2020) and Shipley et~al~(2019) for the small-cavity chambers, and for the Farmer-type chamber, respectively. The detector is positioned at 10 cm depth in a water tank phantom of  $30 \times 30 \times 30~{\rm cm}^3$ . The 7 MV FFF photon beam phase spaces of the Elekta Unity MR-Linac (Elekta Instrument AB Stockholm, Sweden), kindly provided by the manufacturer, are used. The source-to-surface distance (SSD) is set to 133.5 cm. The reference field size is  $10 \times 10~{\rm cm}^2$  and the small field is set to  $1 \times 1~{\rm cm}^2$  at the isocenter for all detectors except for the Farmer type chamber, for which a small field of  $3 \times 3~{\rm cm}^2$  is used to cover the full sensitive volume. The 1.5 T magnetic field is perpendicular to the irradiation beam, consistently with the Elekta Unity MR-Linac.

For the ionization chambers, three detector orientations with respect to the photon beam and the magnetic field are studied. The chamber axis always remains perpendicular to the photon beam and three orientations with respect to the magnetic field are considered: (1) parallel, (2a) perpendicular with the Lorentz force pointing towards the stem, and (2b) perpendicular with the Lorentz force pointing towards the tip, as illustrated in figure 1. For the solid-state detectors, one orientation is studied: (3) the detector axis is parallel to the photon beam and perpendicular to the magnetic field, as shown on the right of figure 1. Only the recommended measurement orientation is considered for the solid-state detectors since the purpose is to evaluate the impact of high-Z components and density for these detectors. In a previous study (Cervantes *et al* 2021), detector dose perturbations in different orientations in these detectors has been investigated.

The magnetic field is implemented with the enhanced electromagnetic field macro (Malkov and Rogers 2016) with the recommended step value of EM ESTEPE = 0.2. The default parameters are used except for the threshold energy for electrons AE = 0.512 MeV and for photons AP = 0.001 MeV. No variance reduction techniques are applied for the electron fluence spectra calculations accordingly to the EGSnrc code recommendations.

For each detector, the electron spectra simulations are performed in three different geometries, as shown in figure 2: (1) the entire detector, (2) the bare cavity with the medium replaced by artificial water, i.e. an artificial medium, denoted  $w^*$ , having the same atomic properties as water including stopping-power density corrections but with the electron density of the original sensitive volume material (i.e. silicon for PTW60012, diamond for PTW60019 and air for the ionization chambers), and (3) the bare cavity filled with water.

To quantify the effect of the magnetic field, the difference between the differential electron fluence at 1.5 T and at 0 T is normalized by the total electron fluence at 0 T:

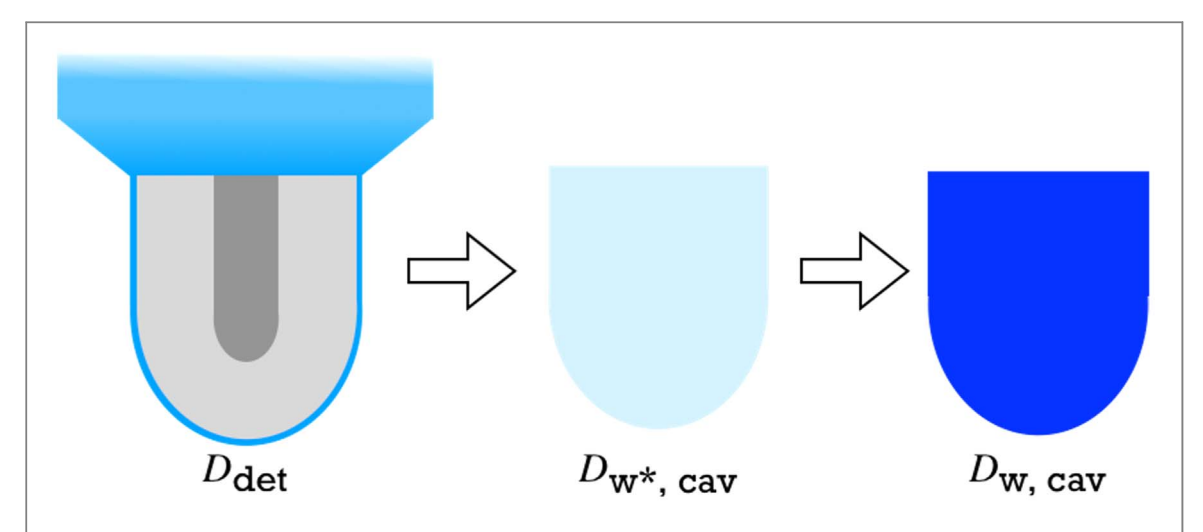
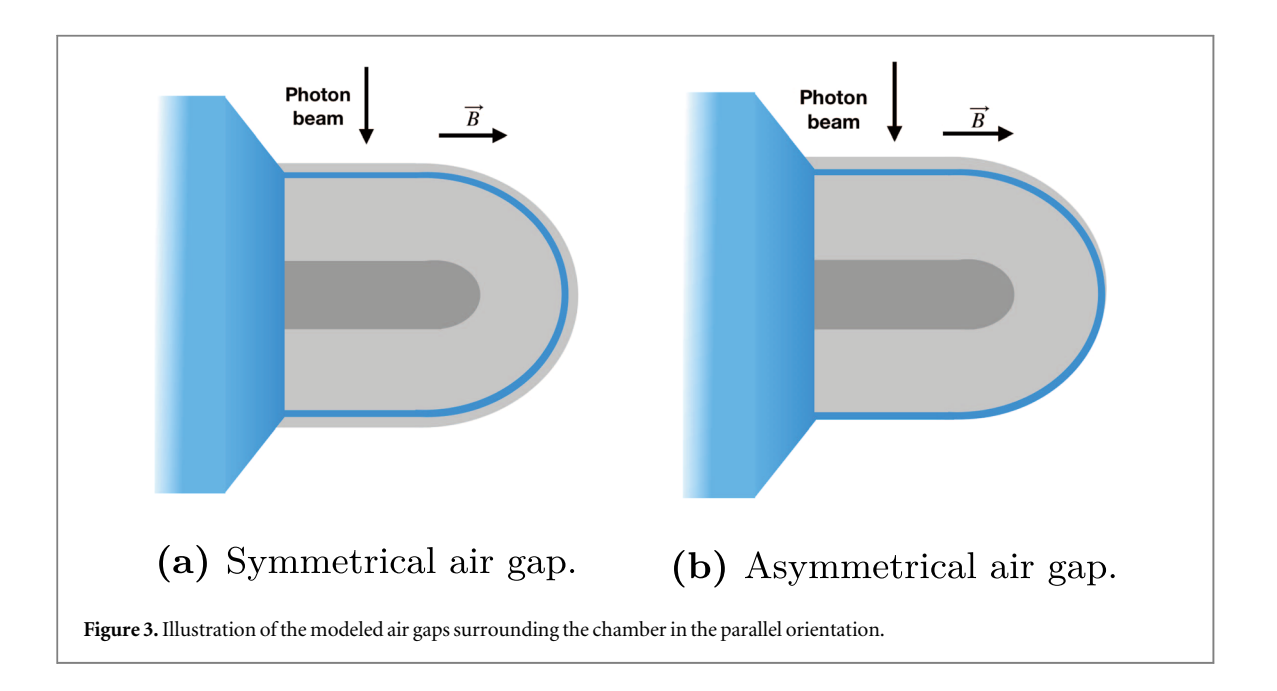


**Figure 2.** Scheme of the three detector geometries where the electron fluence is calculated. On the left, the full detector, on the middle the bare cavity with artificial water  $w^*$ , having the same atomic properties as water with the electron density of the original sensitive volume material, and on the right, the bare cavity filled with water.



$$\Delta_B = \frac{F_e(1.5T) - F_e(0T)}{F_e^{\text{tot}}(0T)}.$$
(11)

For the uncertainty of the electron fluence only the statistical uncertainty from the Monte Carlo simulations is considered.

#### 2.2.3. Presence of air gaps around ionization chambers

In reference dosimetry measurements, air gaps surrounding the detector partially or totally can occur, for instance, between a non-waterproof chamber and its water sleeve or between a chamber and a solid water phantom. In the absence of magnetic fields, the effect of the air gaps has negligible perturbation effects. However, several groups (Hackett *et al* 2016, Malkov and Rogers 2016, Agnew *et al* 2017, O'Brien and Sawakuchi 2017) have shown that these air gaps can strongly affect the chamber response in the presence of an external magnetic field.

Due to the nature of the air gap formation, the location, distribution and size are usually unknown. Diverse situations have been explored, Agnew *et al* (2017) investigated the effect of the location of the air gap around the chamber, Malkov and Rogers (2016) studied the variation of chamber response due to air gaps for multiple magnetic field strengths, and O'Brien and Sawakuchi (2017) investigated the effect of the shape of the air gap, either symmetrical (i.e. with uniform thickness around the chamber) or asymmetrical (i.e. uniform thickness

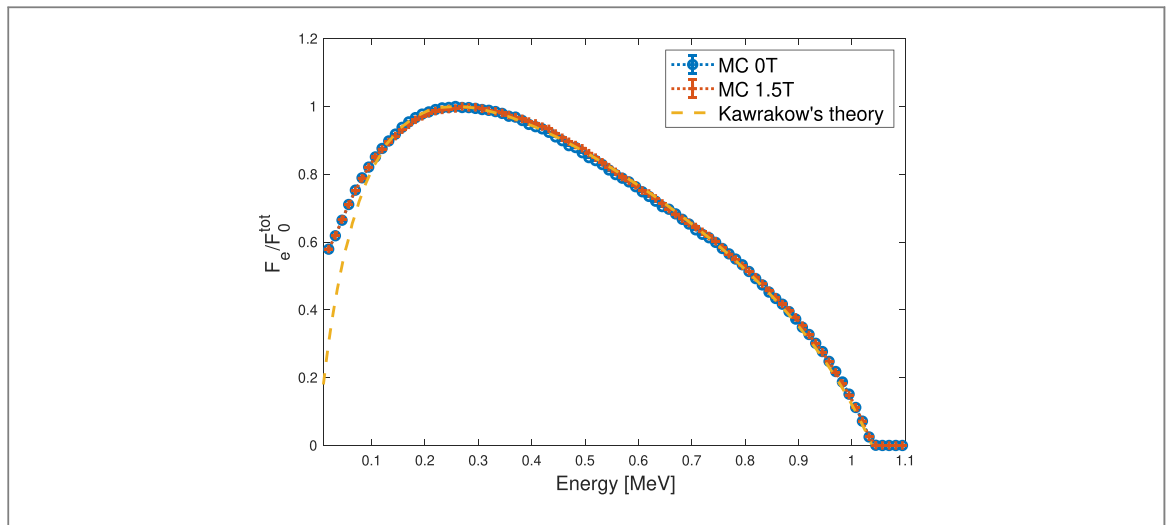
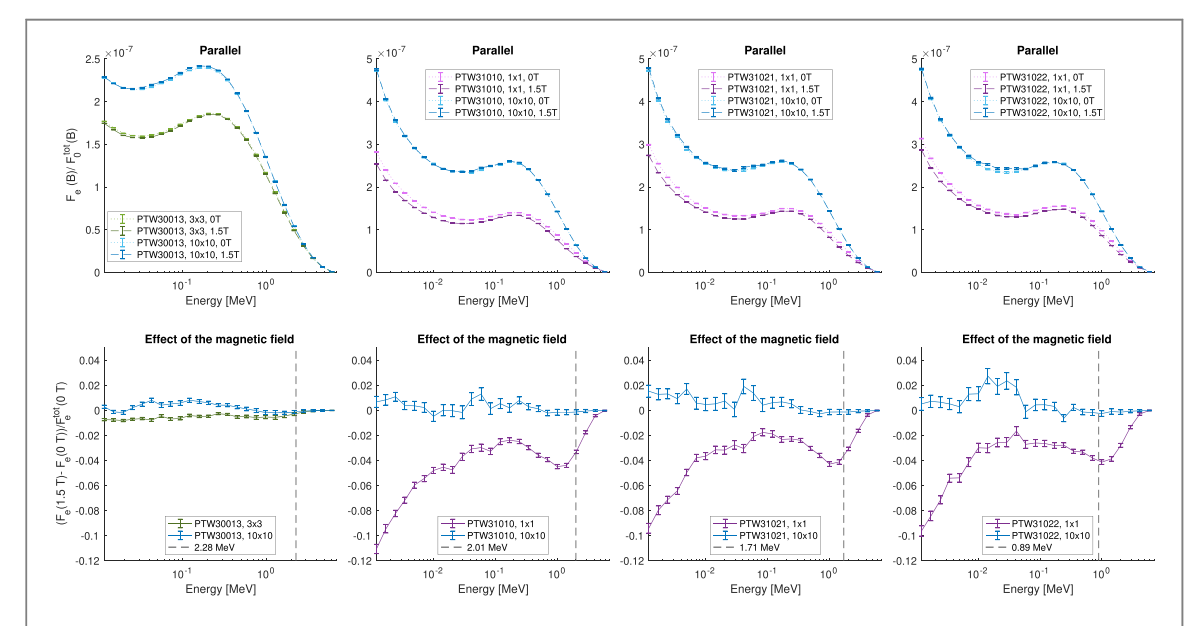


Figure 4. Normalized electron fluence simulated with cavity (EGSnrc) in a water voxel of 1 mm<sup>3</sup> at 0 and 1.5 T and the theoretical prediction from Kawrakow (2000).



**Figure 5.** In the top row, Monte Carlo calculated electron fluence spectra per total incident photon fluence, at 0 and 1.5 T, in each ionization chamber (from left to right: PTW30013, PTW31010, PTW31021 and PTW31022), in the parallel orientation. In the bottom row, the corresponding electron fluence differences due to the presence of the magnetic field in each field size and chamber model. The vertical dashed line is at the energy at which the gyration radius equals the cavity diameter, explained in section 3.4.

but only in one side of the chamber). Most of the studies were performed for Farmer-type chambers. In this study, the effect of symmetrical and asymmetrical air gaps on chamber response in a Farmer-type chamber and in a smaller chamber, the semiflex PTW31010 is evaluated via the calculation of electron fluence spectra.

The influence of air gaps surrounding the detectors is evaluated in the same experimental setup described previously. The Monte Carlo calculations are performed in two chambers (PTW30013 and PTW31010) for a reference field, at 0 and 1.5 T, in the parallel orientation. Considering two types of air gaps: (1) symmetrical air gaps are modelled as air layers with uniform thickness (0.2 mm, 0.5 mm, 1.0 mm and 1.5 mm) surrounding the chamber, and (2) asymmetrical air gaps are modelled as air layers with uniform thickness (0.2 mm, 0.5 mm, 1.0 mm and 1.5 mm) placed only in the upper part of the chamber, as shown in figure 3. The air gap effect with or without magnetic fields is evaluated with the electron fluence spectral difference:

$$\Delta_{\text{air gap}}(B_i) = \frac{F_{e,\text{airgap}}(B_i) - F_{e,\text{noairgap}}(B_i)}{F_{e,\text{noairgap}}^{\text{tot}}(B_i)},$$
(12)

with  $B_i$  either 0 T or 1.5 T and  $F_{e,\text{noairgap}}^{\text{tot}}$  the total electron fluence when there is no air gap.

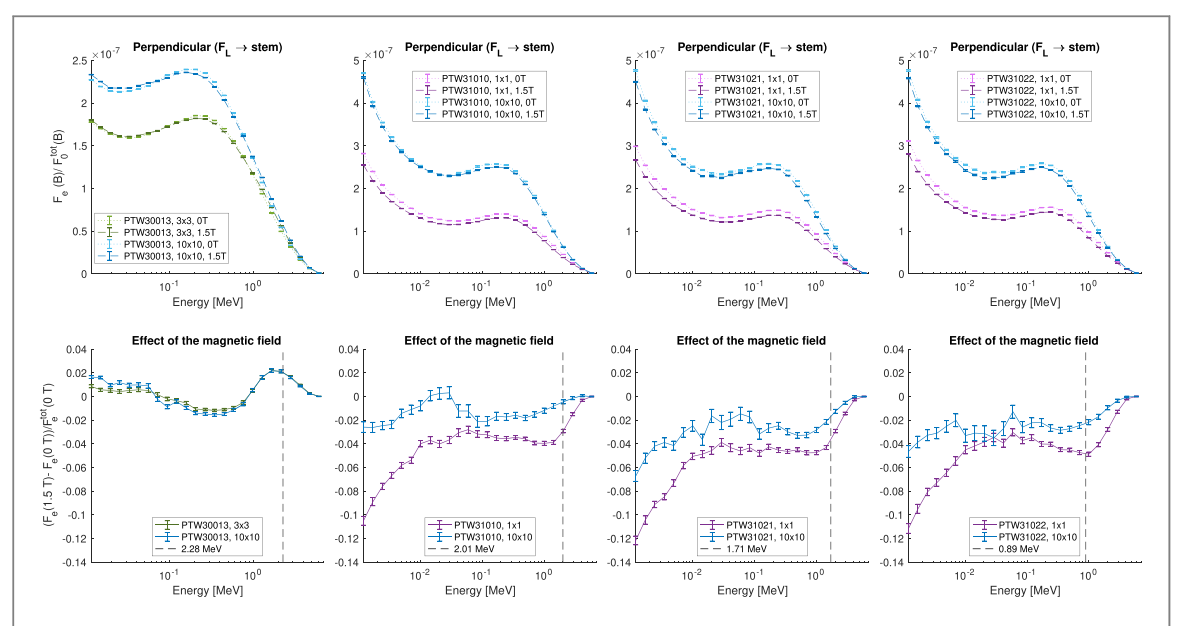


Figure 6. In the top row, Monte Carlo calculated electron fluence spectra per total incident photon fluence, at 0 and 1.5 T, in each ionization chamber (from left to right: PTW30013, PTW31010, PTW31021 and PTW31022), in the perpendicular orientation 2a ( $\mathbf{F}_L \rightarrow \text{stem}$ ). In the bottom row, the corresponding electron fluence differences due to the presence of the magnetic field in each field size and chamber model. The vertical dashed line is at the energy at which the gyration radius equals the cavity diameter, explained in section 3.4.

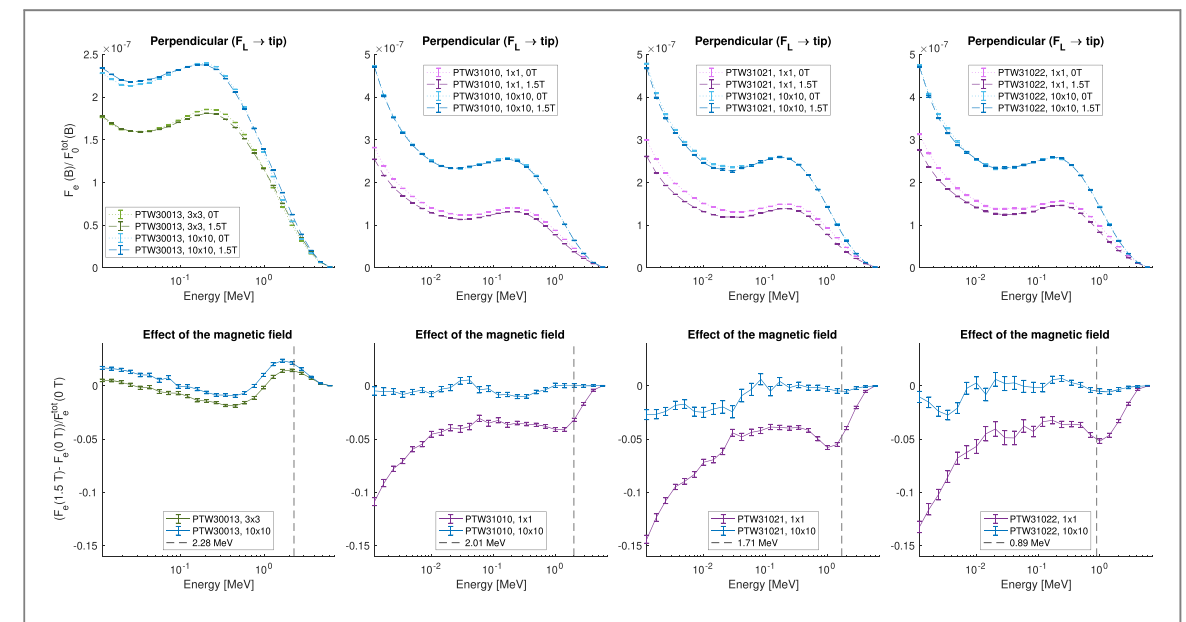


Figure 7. In the top row, Monte Carlo calculated electron fluence spectra per total incident photon fluence, at 0 and 1.5 T, in each ionization chamber (from left to right: PTW30013, PTW31010, PTW31021 and PTW31022), in the perpendicular orientation 2b ( $F_L \rightarrow tip$ ). In the bottom row, the corresponding electron fluence differences due to the presence of the magnetic field in each field size and chamber model. The vertical dashed line is at the energy at which the gyration radius equals the cavity diameter, explained in section 3.4.

## 3. Results and discussion

#### 3.1. Validation of Monte Carlo calculations of electron fluence in the presence of magnetic fields

If Fano conditions are fulfilled, electron fluence spectra in the presence of a magnetic field are identical to the electron fluence spectra in the absence of magnetic fields. Therefore, the Monte Carlo calculations of electron fluence spectra at 1.5 T can be validated against the electron fluence spectra at 0 T. For this, a geometry fulfilling the first special Fano condition is simulated, the comparison between Monte Carlo simulations of electron fluence in the absence and presence of an external magnetic field is shown in figure 4. The agreement is good and consistent with the statistical uncertainty of the simulations (<0.1%). An additional comparison with Kawrakov's analytical approximation (Kawrakow 2000) is presented.

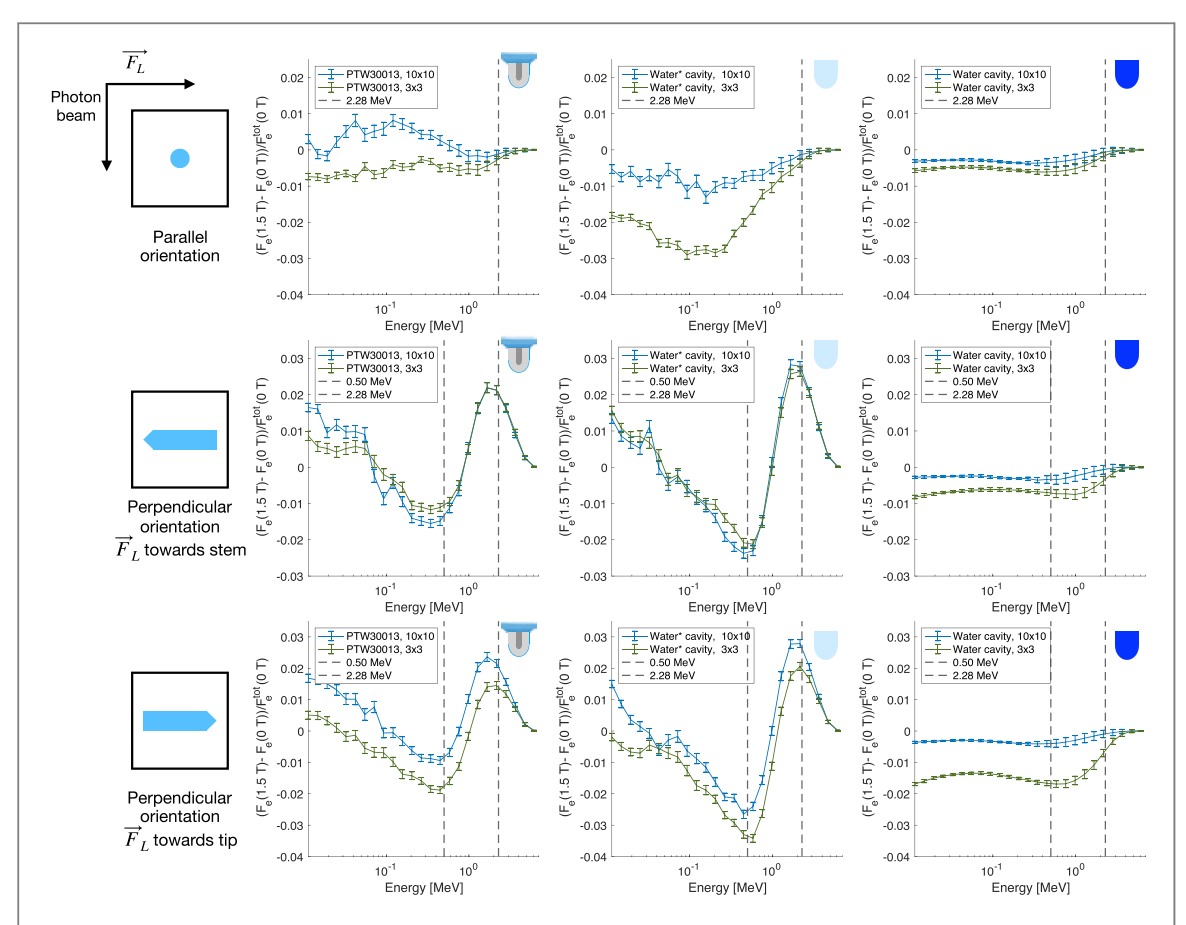


Figure 8. The electron fluence spectral differences due to the magnetic field in each Farmer-type chamber geometry considered in the parallel orientation on the top row and perpendicular orientations with  $F_L$  pointing towards the stem on the middle row and  $F_L$  pointing towards the tip on the bottom row. The geometries are the Farmer type chamber (left), the bare cavity with artificial water (middle) and the bare cavity filled with water (right) at 0 and 1.5 T for fields of  $10 \times 10$  cm $^2$  and  $3 \times 3$  cm $^2$ . The vertical dashed line at the energy (2.28 MeV) at which the gyration radius equals the cavity diameter. The vertical dashed line at the energy (0.50 MeV) at which  $\Delta l = 0$ . Both dashed lines are explained in section 3.4. On the left, an illustration of the sensitive volume in the smallest field size in each orientation.

**Table 2.** Percentage of total electron fluence variation due to the magnetic field in the ionization chambers.

		Parallel	$\begin{array}{c} \text{Perpendicular} \\ (F_L \rightarrow \text{ stem}) \end{array}$	$\begin{array}{c} \text{Perpendicular} \\ (\textbf{F}_{L} \rightarrow \ \text{tip}) \end{array}$
PTW30013	$10 \times 10 \mathrm{cm}^2$	$-0.08 \pm 0.00\%$	$4.42 \pm 0.00\%$	$5.12 \pm 0.00\%$
	$3 \times 3  \text{cm}^2$	$-1.24 \pm 0.00\%$	$4.75\pm0.00\%$	$2.35\pm0.00\%$
PTW31010	$10 \times 10  \text{cm}^2$	$0.14\pm0.00\%$	$-2.56 \pm 0.00\%$	$-0.24 \pm 0.00\%$
	$1 \times 1 \text{ cm}^2$	$-11.60 \pm 0.03\%$	$-10.62 \pm 0.03\%$	$-11.39 \pm 0.03\%$
PTW31021	$10 \times 10  \text{cm}^2$	$-0.19 \pm 0.00\%$	$-6.08 \pm 0.01\%$	$-1.27 \pm 0.00\%$
	$1 \times 1  \text{cm}^2$	$-10.56 \pm 0.03\%$	$-11.85 \pm 0.03\%$	$-14.50 \pm 0.04\%$
PTW31022	$10 \times 10  \mathrm{cm}^2$	$-0.18 \pm 0.00\%$	$-4.58 \pm 0.01\%$	$-0.90 \pm 0.00\%$
	$1 \times 1  \text{cm}^2$	$-9.96 \pm 0.04\%$	$-11.08 \pm 0.04\%$	$-12.34 \pm 0.04\%$

# 3.2. Electron fluence in ionization chambers

Electron fluence spectra normalized by the total incident photon fluence are scored in each ionization chamber for a reference and a small field, at 0 and 1.5 T, in the parallel and in the two perpendicular orientations, results are shown in the top row of figures 5, 6 and 7. The spectral differences due to the magnetic field (equation (11)) are presented in the bottom row of each figure. Additionally, the variation in the total electron fluence due to the magnetic field is presented in table 2. In the three orientations, the magnetic field impact is more significant in small fields than in the reference field in all chambers, but it is especially relevant in the small-cavity chambers.

In small fields, the electron fluence decreases at 1.5 T compared to the 0 T case. In particular, in the small-cavity chambers, the electron fluence decreases with decreasing energy. This is in agreement with the reduction

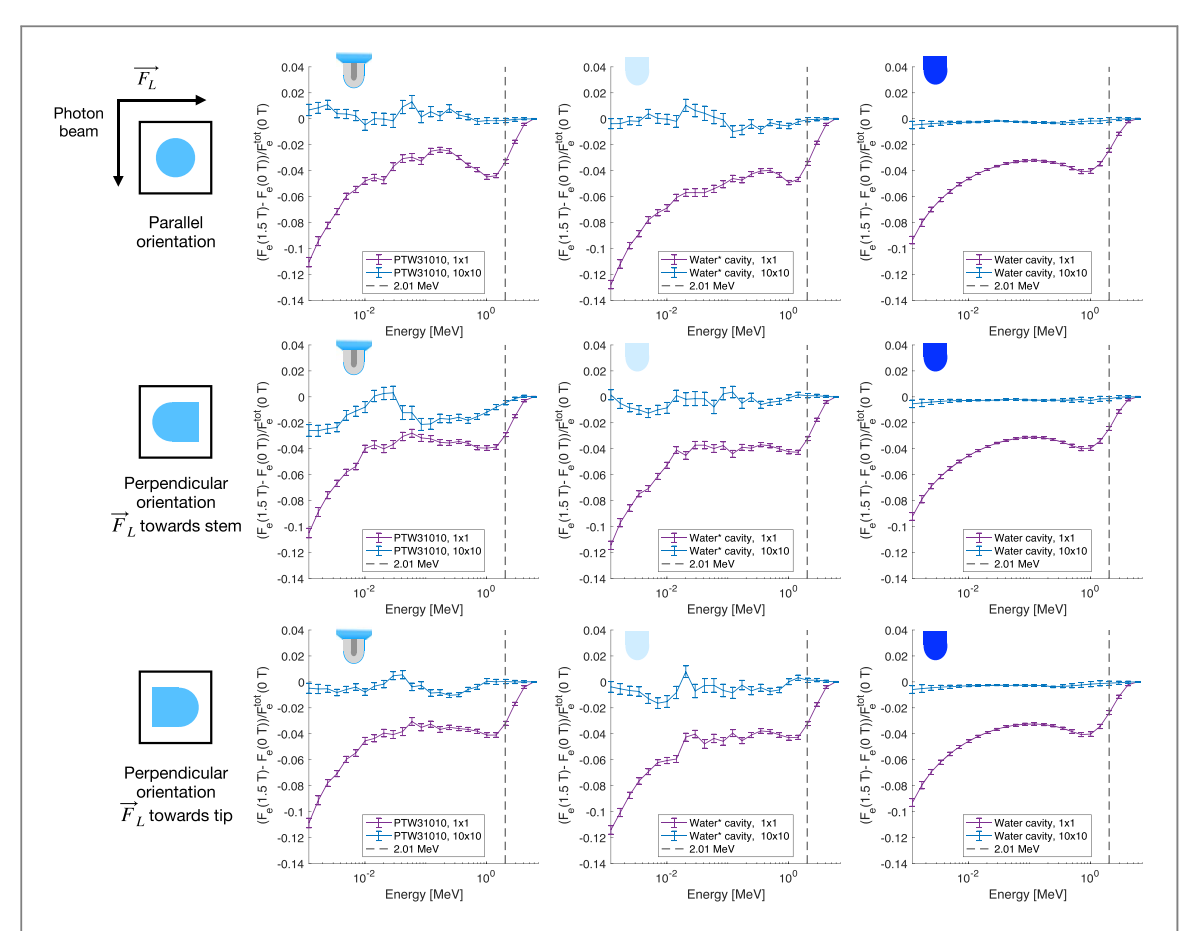


**Figure 9.** The electron fluence spectral differences due to the magnetic field in each semiflex chamber geometry considered in the parallel orientation on the top row and perpendicular orientations with  $F_L$  pointing towards the stem on the middle row and  $F_L$  pointing towards the tip on the bottom row. The geometries are chamber (left), the bare cavity with artificial water (middle) and the bare cavity filled with water (right) at 0 and 1.5 T for fields of  $10 \times 10 \text{ cm}^2$  and  $1 \times 1 \text{ cm}^2$ . The vertical dashed line is at the energy at which the gyration radius equals the cavity thickness, explained in section 3.4. On the left, an illustration of the sensitive volume in the smallest field size in each orientation.

in absorbed dose previously observed in the presence of a magnetic field (O'Brien *et al* 2016, van Asselen *et al* 2018) because electrons deposit their energy closer to the point where they are created due to the Lorentz force (de Pooter *et al* 2020).

The electron fluence spectra vary with orientation; the magnetic field influence is more significant in the perpendicular orientations because there are larger perturbations coming from the extracameral components than in the parallel orientation. In orientation 2a, electrons, on average, are deflected towards the stem, while in orientation 2b, they are deflected towards the tip. In magnetic fields, the total fluence is reduced up to 11.6% in the parallel orientation and up to 14.50% in the perpendicular orientations.

Another effect of the extracameral components can be observed in chamber PTW31021; there is a reduction in the low-energy electrons for both field sizes. This is due to the presence of an inner air layer between the graphite and the PMMA wall, as pointed out previously in Cervantes  $et\,al\,(2020)$ .

The magnetic field effect on electron spectra follows a similar trend in the small-cavity chambers in all orientations. On the contrary, there is a different trend between the parallel and the perpendicular orientations for the Farmer-type chamber. The magnetic field effect is more or less constant in the parallel orientations, while in the perpendicular orientation, the variations with energy are more important. This is mainly due to the cavity length and is discussed in detail in the following sections.

#### 3.3. Effect of detector geometry and density

## 3.3.1. Farmer-type chamber

Electron fluence spectral differences due to the presence of an external magnetic field for two irradiation fields  $(10 \times 10 \text{ cm}^2 \text{ and } 3 \times 3 \text{ cm}^2)$  in the Farmer-type chamber geometries, in all orientations, are presented in figure 8. The three different geometries are the cavity of the full detector (left), the bare cavity filled with artificial water  $w^*$  (middle) and the bare cavity filled with water (right).

In the parallel orientation, shown in the top row of figure 8, the magnetic field has a stronger impact in the small field than in the reference field in the three chamber geometries. The largest fluctuations occur for the

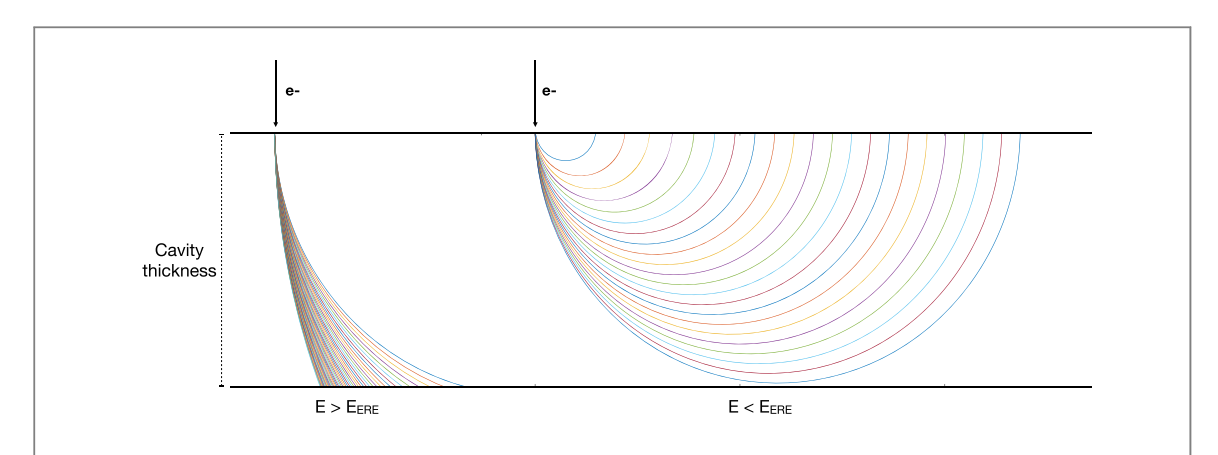


**Figure 10.** Electrons entering an infinite slab at the same position in a vacuum in the presence of an external 1.5 T magnetic field. *E*<sub>ERE</sub> is the energy at which the gyration radius equals the cavity thickness. On the left, electrons with enough energy to fully traverse the slab. On the right, electrons with energy to return to the incident wall.

second geometry (middle), i.e. when the only difference between the cavity and the medium is the density, especially for the small field. These results confirm that the density is one of the main causes for the small-field effects as previously seen in the absence of magnetic fields (Scott  $et\,al\,2012$ ) and in the presence of magnetic fields (Cervantes  $et\,al\,2021$ ). The perturbations mainly come from low-energy electrons since in a constant magnetic field, the lower the energy, the smaller is the gyration radius which results in an increase in the magnetic field term in the radiation transport equation (equation (3)). Note that the perturbations in the full chamber geometry (left) are smaller than in the  $w^*$  geometry; this indicates that the extracameral components perturbations are in the opposite direction, i.e. they increase the electron fluence which compensates the density perturbations.

In the perpendicular orientations, shown in the middle and bottom rows of figure 8, there are no significant variations for the water cavity. For the other two geometries, the magnetic field effect varies considerably with energy, and it does not vary significantly with field size. In this case, the cavity is so large that low-energy electrons deposit their energy locally, and perturbations from lateral electrons are less significant, which explains the lack of small-field effects.

The general trend of the magnetic field effect comes mainly from the density differences, as can be seen in the middle column of figure 8. The trend variations are due to the cavity dimensions, and the explanation is in section 3.4. As in the parallel orientation, perturbations are smaller for the full chamber (left) because the extracameral components are compensating the electron loss, especially at low energies.

The variations on electron fluence are smaller in the parallel orientation than in the perpendicular orientations because the extracameral components play a more critical role in the perpendicular orientations, which the Farmer chamber length emphasizes.

## 3.3.2. Small-cavity chambers

The differences in electron fluence due to the magnetic field are similar in the three small-cavity chambers in all orientations. They are shown in figure 9 only for the chamber PTW31010 and its corresponding geometries. The magnetic field impact depends strongly on chamber geometry, the Farmer-type chamber and the small-cavity chambers are impacted differently. There are two main geometrical differences between these types of chambers: the length of the cavity (see table 1) and the shape of the tip, which is semi-spherical for the small-cavity chamber and conical pointed for the Farmer chamber.

For the reference field, the magnetic field effect fluctuates around zero with spectral differences within 1.5% in all orientations except in orientation 2a for the full chamber geometry (left). The reason being that the stem perturbations increase in this orientation; electrons are, on average, deflected towards the stem reducing the electron fluence, especially the low-energy electrons.

When the chamber is irradiated with the reference field, there is charged particle equilibrium (CPE), and if the sensitive volume is filled with water, then the first special Fano condition is fulfilled. Hence, the electron fluence remains the same in the absence and presence of a magnetic field, as shown in the right of figure 9. In contrast, when the irradiation field size decreases, the electron fluence decreases significantly with decreasing energy in the presence of magnetic fields. The fluence reduction is due to the loss of lateral CPE in small fields, which is amplified by the asymmetry introduced by the Lorentz force.

When the cavity electron density equates that of air (middle), the magnetic field effect follows the same trend as in the water sensitive volume, but the electron fluence is further reduced in this case. Density perturbations

Figure 11. Illustration of each chamber sensitive volume inside the smallest field. The dimensions of the sensitive volume and the field are to scale.

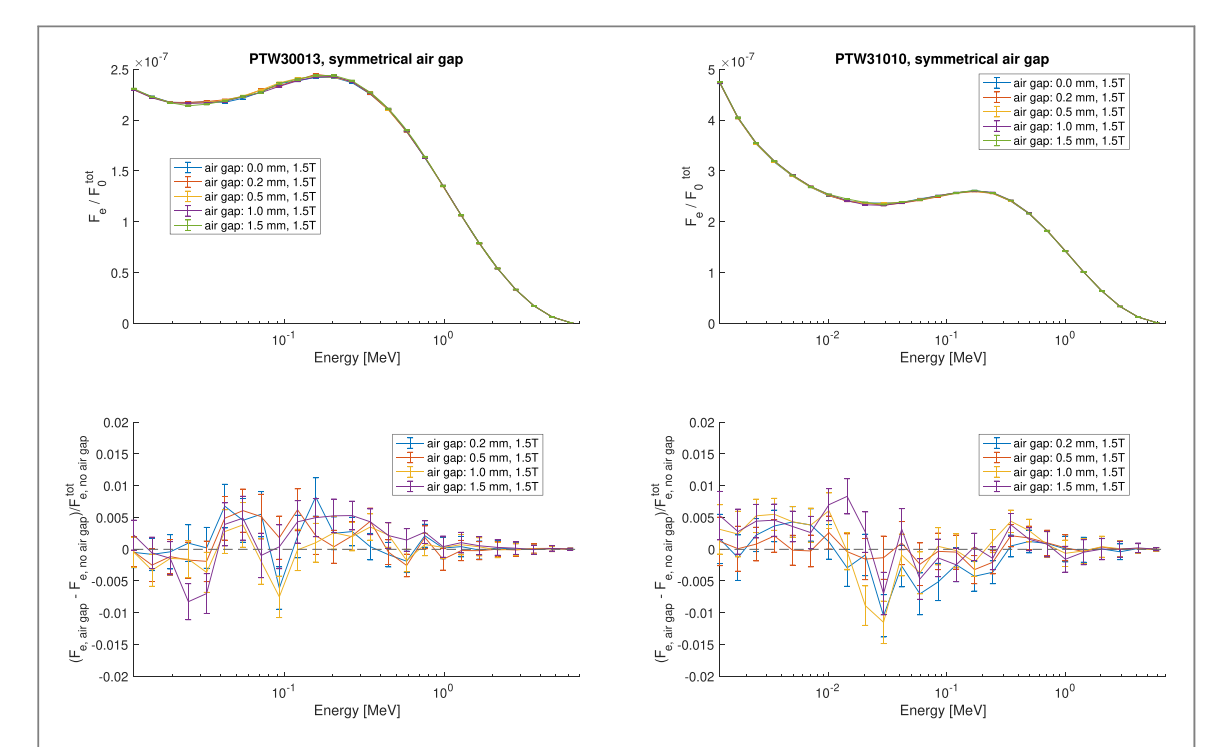


**Figure 12.** Symmetrical air gaps around chambers PTW30013 (left) and PTW31010 (right) at 1.5 T. In the top row, the electron fluence spectra per total incident photon fluence in the chamber for air gaps of different thicknesses. In the bottom row, the effect of the air gap is evaluated with respect to no air gap in the electron fluence in the presence of magnetic fields.

increase in the presence of magnetic fields (Cervantes  $et\,al\,2021$ ), in low-density materials, fewer secondary electrons are produced, and the electron mean free path generally increases, thus becoming susceptible to the Lorentz force.

When the full chamber (left) is simulated, the magnetic field impact also follows the same trend as in the other two geometries for small fields. However, there are slight variations associated with the influence of extracameral components that changes with orientation. In general, the perturbations are smaller, as the extracameral components seem to compensate the electron fluence reduction.

# 3.4. Effect of the cavity size

The cavity size is relevant for small fields dosimetry in the absence and presence of magnetic fields. The relation between the cavity size and the magnetic field can be approached by considering an electron travelling in vacuum through an infinite slab with the same thickness as the cavity, as shown in figure 10. Depending on its energy, an electron can either traverse the cavity (left of figure 10) or it can fully return to the incident wall (right of figure 10). The behaviour change occurs when the gyration radius is equal to the cavity thickness at a certain energy, named  $E_{\rm ERE}$ . This ERE energy is presented as a dashed line for each detector in figures 5–16(b). In these figures, for the magnetic field effect at small fields, the ERE energy is near the convex region at high energies where there is a local minimum. Note that the ERE energy is only an approximation, and the true scenario is much more complex: electrons enter the cavity in different positions, electrons interact with the medium and

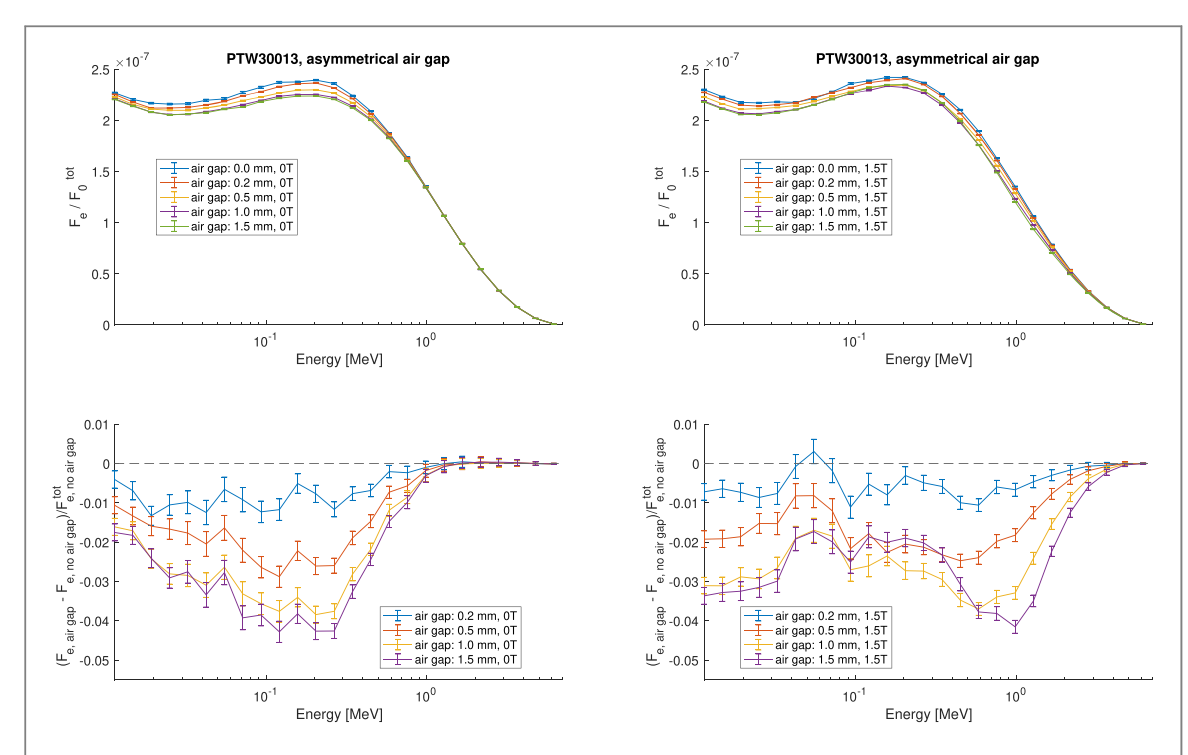


**Figure 13.** Asymmetrical air gaps around the Farmer-type chamber at 0 T (left) and at 1.5 T (right). In the top row, the electron fluence spectra per total incident photon fluence in the chamber for air gaps of different thicknesses. In the bottom row, the effect of the air gap is evaluated with respect to no air gap.

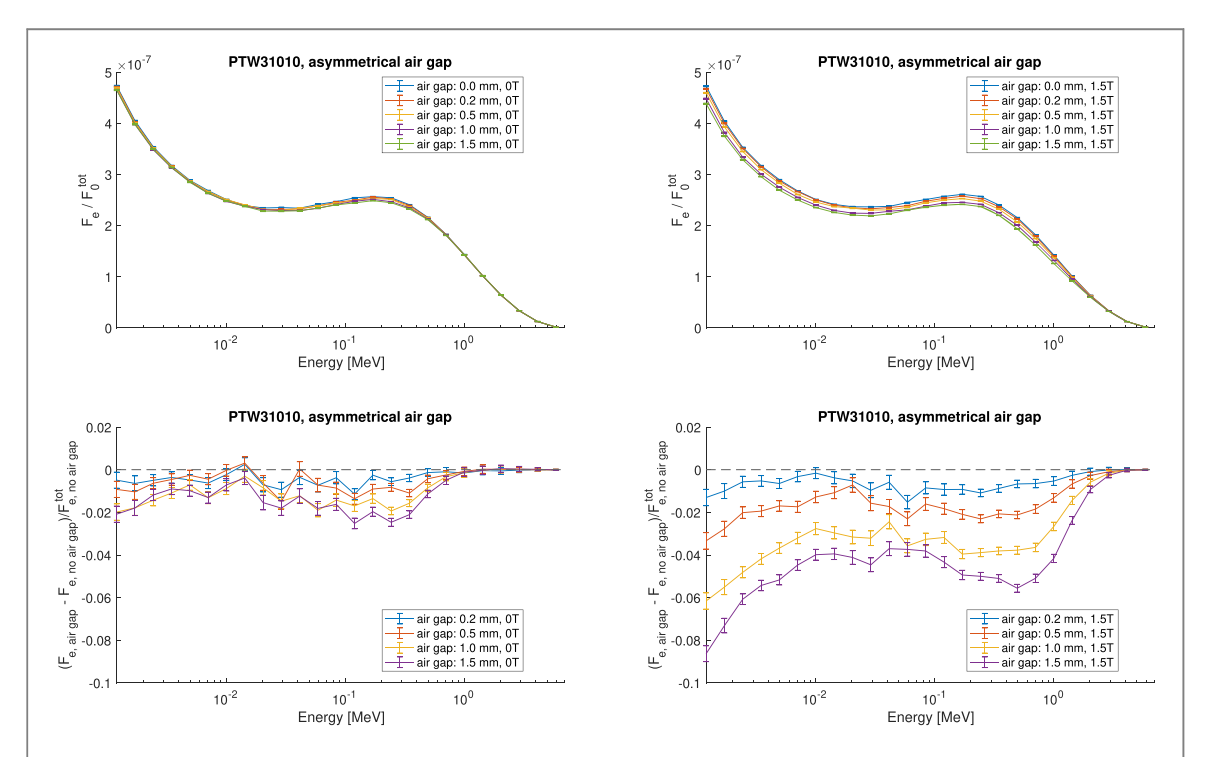


**Figure 14.** Asymmetrical air gaps around the PTW31010 chamber at 0 T (left) and at 1.5 T (right). In the top row, the electron fluence spectra per total incident photon fluence in the chamber for air gaps of different thicknesses. In the bottom row, the effect of the air gap is evaluated with respect to no air gap.

lose energy, there is lateral gain and loss of electrons, the thickness cavity is not uniform, and the fluence varies with detector orientation.

In the parallel orientation, electrons coming in the main direction encounter a plane with approximately the same thickness and length (i.e. sensitive diameter of table 1), as illustrated on the left figure of 11. Whereas, in the perpendicular orientation, the encountered plane has a thickness equal to the sensitive volume diameter and the

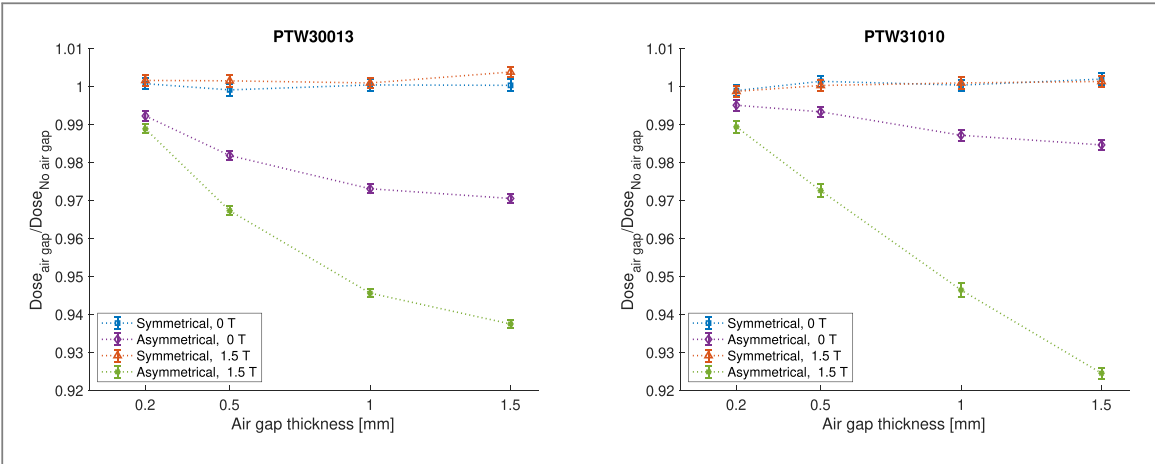


Figure 15. Ratio of dose in the cavity with an air gap relative to that with no air gap at 0 and 1.5 T for chambers PTW30013 (left) and PTW31010 (right).

length of the sensitive volume, as illustrated on the right of figure 11. For the pinpoint 3D (PTW31022) and the semiflex 3D (PTW31021), the diameter and length of the sensitive volume are equal, the semiflex (PTW31010) is slightly longer than wider, and the Farmer chamber is almost four times longer than wider. The latter case approaches the infinite slab geometry in the perpendicular orientation and explains the remarkable trend change of the Farmer between the parallel and perpendicular orientation.

To explain the magnetic field effect trend in the Farmer chamber in the perpendicular orientation, see figure 8, the cavity can be approximated to an infinite slab where only the effect of the magnetic field is considered. Then a pathlength correction,  $\Delta l$ , due to the magnetic field can be defined as

$$\Delta l = \pi * R - d,\tag{13}$$

where  $\pi * R$  is the electron pathlength in magnetic fields, and d is the electron pathlength in the absence of magnetic fields which is equal to the cavity thickness. For energies below  $E_{\rm ERE}$ , three cases can occur

If  $\Delta l$  < 0, then the electron pathlength is smaller in magnetic fields than without it.

If  $\Delta l = 0$ , then the electron pathlength is the same with and without magnetic fields.

If  $\Delta l > 0$ , then the electron pathlength is bigger in magnetic fields than without it.

The variation of  $\Delta l$  explains the trend of magnetic field effect, the minimum of the curves in the middle and bottom row of figure 8 occurs close to the energy at which  $\Delta l=0$ . For the chamber PTW30013 dimensions, this energy is 0.50 MeV. Even though these cases depict a simplistic scenario, they provide a good enough approximation of the full radiation transport scenario.

It is worth noting that such a simplistic scenario cannot fully explain the perturbation effects of any radiation detector. While evaluating pathlength differences with an infinite slab might be valuable in large air cavities, for small cavities, it cannot suffice since the geometry is more complex with a central electrode and a wall tip in the vicinity, which produces additional electrons entering the cavity for which the trajectory cannot be addressed analytically. For solid detectors, the situation is even more complex. In such cases, one needs to fully consider what transport equation implicates and how the electron fluence is perturbed compared to ideal conditions, such as in Fano conditions. Unfortunately, in the presence of homogeneous magnetic fields, Fano's theorem cannot hold, and therefore conventional simplifications cannot be used. Monte Carlo remains the only valid method to approach this problem.

#### 3.5. Air gap effect on electron fluence spectrum

#### 3.5.1. Symmetrical air gaps

The influence of the symmetrical air gaps on electron fluence is presented in figure 12 for the Farmer chamber and the semiflex chamber. In general, there are no significant differences among the thicknesses considered, and the air gap effect on electron fluence is 1% or less with respect to the no air gap case for all thicknesses for both chambers.

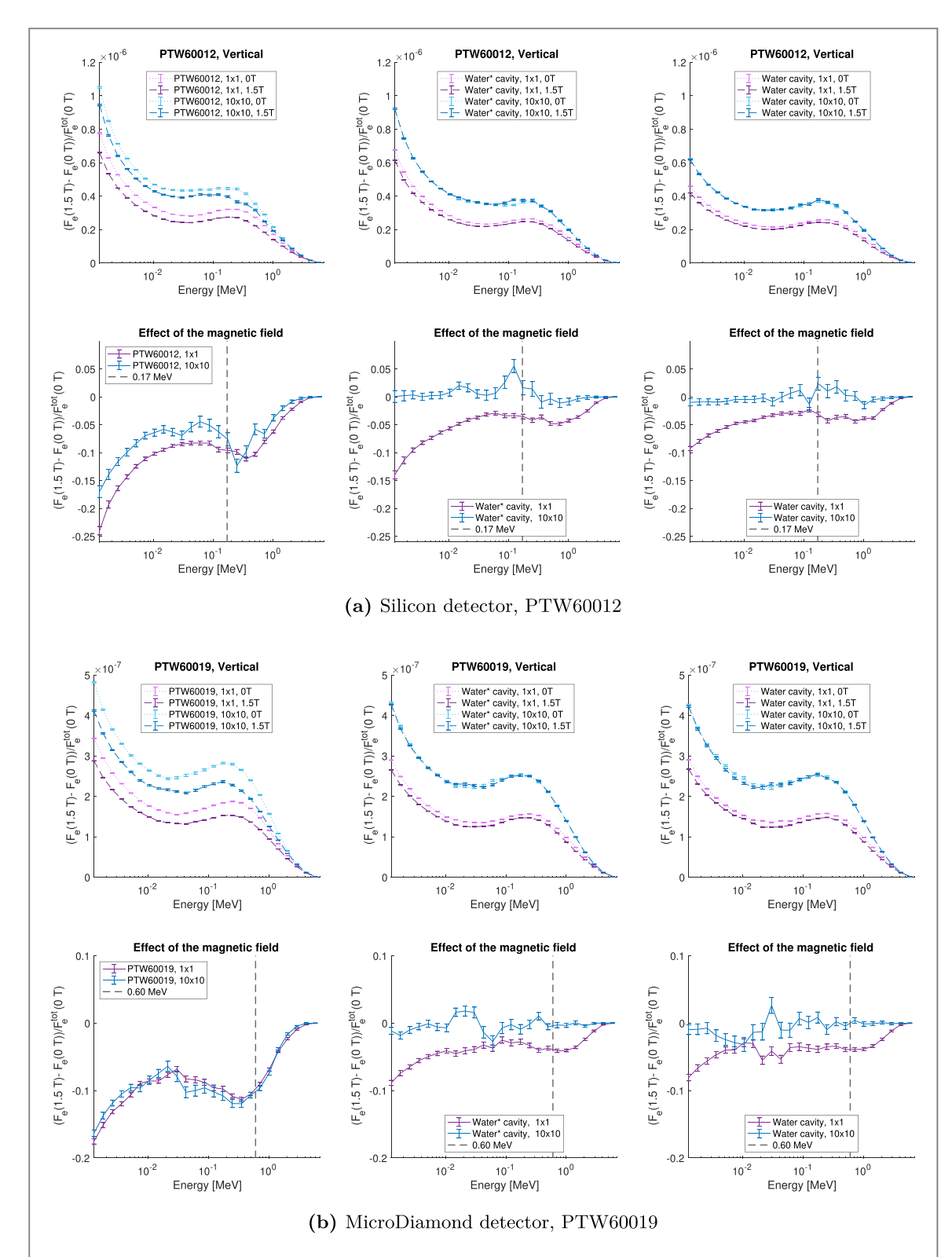


Figure 16. In the top row, the electron fluence per incident photon fluence for the full solid-state detector (top left), for the bare cavity with artificial water (top middle) and for the bare cavity filled with water (top right) at 0 and 1.5 T for square irradiation beams of  $10 \times 10 \, \mathrm{cm}^2$  and  $1 \times 1 \, \mathrm{cm}^2$ . In the bottom row, the relative difference between the electron fluence at 0 and 1.5 T for each field size and each geometry considered. The vertical dashed line is at the energy at which the gyration radius equals the cavity thickness, explained in section 3.4.

# 3.5.2. Asymmetrical air gaps

The electron fluence spectra normalized by the total incident photon fluence at 0 and 1.5 T for chamber PTW30013 surrounded by an asymmetrical gap are shown in figure 13. Even in the absence of magnetic fields, there is an air gap effect, and the fluence perturbations increase with air gap thickness. In the presence of an

**Table 3.** Percentage of total electron fluence variation due to the magnetic field in the ionization chambers surrounded by an air gap. The uncertainty is below 0.01% in all cases.

Air gap Thickness [mm]	PTW	730013	PTW31010		
	Symmetrical [%]	Asymmetrical [%]	Symmetrical [%]	Asymmetrical [%]	
0.2	0.04	-0.75	-0.31	-0.83	
0.5	0.02	-2.25	-0.19	-2.44	
1.0	-0.04	-4.08	-0.25	-4.73	
1.5	0.08	-5.13	-0.45	-7.04	

external magnetic field, illustrated on the right of figure 13, there is a further reduction of low-energy electrons; the reduction becomes more pronounced with increasing air gap thickness.

The results for the asymmetrical air gap surrounding the small-cavity chamber are presented in figure 14. In this case, the electron fluence perturbations are 2.52% or less at 0 T and they decrease as much as 8.63% at 1.5 T. The influence of the magnetic field is present along all the energy spectrum, but it increases, once again, at low-energies. The presence of asymmetrical air gaps has a bigger impact in chambers with smaller cavity sizes in the presence of an external magnetic field.

#### 3.5.3. Chamber dose response

In the case of symmetrical air gaps, the 1% variation in electron fluence due to the magnetic field corresponds to a variation of the chamber dose responses within 0.5% as shown in figure 15. These results are consistent with O'Brien and Sawakuchi (2017), where results showed that symmetrical air gaps around the chambers have a minimal effect.

For the case of asymmetrical air gaps, the variation in electron fluence in the Farmer chamber corresponds to a maximal dose reduction of 2.95% and 6.26%, at 0 T and 1.5 T, respectively, as observed in figure 15. For the small-cavity chamber, the dose is further reduced, by as much as 7.55% in a magnetic field, as shown in figure 15.

The total fluence variation due to the presence of the magnetic field in all the air gap cases is presented in table 3.

## 3.6. Solid-state detectors

The electron fluence spectra normalized by the total incident photon fluence in the solid-state detectors are only calculated in orientation 3, in which the detector axis is aligned with the photon beam, and it is perpendicular to the magnetic field. These spectra are calculated in three detector geometries (shown in figure 2) in two square fields  $10 \times 10 \text{ cm}^2$  and  $1 \times 1 \text{ cm}^2$  for 0 T and 1.5 T, the results are presented in the top rows of figures 16(a) and (b) for the silicon diode and the microDiamond detector, respectively. The corresponding spectral differences due to the magnetic field are presented in the bottom row of each figure.

The electron fluence decreases in both solid-state detectors in the presence of magnetic fields, as shown on the left columns of figures 16(a) and (b). The effect is very similar in both field sizes for the silicon diode and almost identical for the microDiamond detector, indicating the strong magnetic field impact even in large field sizes, as previously seen in Cervantes *et al* (2021). The magnetic field effect is more pronounced for the low-energy electrons.

When comparing the effect of the magnetic field in the full geometry to the one in the water\* cavity, the behaviour is different, particularly in the reference field. Perturbations seem to be strongly amplified by the extracameral components. The density effect can be evaluated by comparing the spectra in the second and third geometry (middle and right columns of figures 16(a) and (b)). The trends are very similar for each field size, agreeing with previous results (Cervantes *et al* 2021) where it was shown that the magnetic field effect on the density perturbation factors is not significant, 1% or less in the dose response. Differences in behaviour between the two field sizes come from the lack of lateral CPE in small fields that is amplified by the asymmetry introduced by the Lorentz force.

# 4. Summary

Electron fluence spectra have been calculated for six detectors in a reference field and in a small field, in different orientations, in the absence and presence of a magnetic field. The magnetic field effect in the electron fluence in each detector was different. To identify the underlying mechanism behind the magnetic field impact, additional

calculations of the electron fluence were performed in two modified detector geometries: the bare sensitive volume filled with artificial water having the same electronic density as the original material,  $w^*$ , and filled with water. In solid-state detectors, the extracameral component perturbations increase in the presence of a magnetic field. In ionization chambers, the density variations increase the electron fluence perturbations in the presence of magnetic fields, as previously observed in Cervantes *et al* (2021).

Three chamber orientations are investigated, the variation in total electron fluence due to the magnetic field is presented in table 2. In the Farmer chamber case, the magnetic field impacts less in the parallel orientation than in the perpendicular orientation. In the latter, the interplay between the gyration radius and the cavity size (the cavity length is 3.77 times larger than the cavity diameter) dramatically affects the electron fluence, as explained in section 3.4.

For the small-cavity chambers, in the reference field, the magnetic field impact on total electron fluence drastically increases when the Lorentz force points towards the chamber stem. A smaller effect appears in the other two orientations. Contrary to the Farmer chamber, the cavity length is comparable to the cavity diameter in these chambers, explaining the similar behaviour among these two orientations. A significant impact of the small field size is observed in the small-cavity chambers (note that the narrow field used in the Farmer-type chamber is not that small) for all orientations; the magnetic field reduces the total electron fluence between 9.96% and 14.50% depending on the orientation.

The cases of symmetrical and asymmetrical air gaps (thicknesses between 0.2 and 1.5 mm) surrounding a Farmer chamber and a small-cavity chamber are also investigated. The variation in the total electron fluence due to the magnetic field in these cases are presented in table 3. For all the symmetrical air gaps, the variation is equal or below 0.08% for the Farmer chamber and below 0.5% for the semiflex. In the case of the asymmetrical air gaps, the magnetic field effect in total fluence increases with the gap thickness up to -5.13% and 7.04% for the Farmer chamber and semiflex chamber, respectively.

The magnetic field strongly impacted the solid-state detectors in both field sizes. The total fluence is reduced by as much as  $-15.06\pm0.09\%$  and  $-16.00\pm0.07\%$  for the silicon diode and the microDiamond, respectively. The high-density extracameral components seem to be responsible for the strong effect of the magnetic field.

#### 5. Conclusion

This investigation provides physical insights on the response of different detectors—one Farmer chamber, three small-cavity chambers and two solid-state detectors—when irradiated with megavoltage photon beams coupled to an external magnetic field. The electron fluence differential in energy in the detector cavity can be severely modified in magnetic fields, and fluence perturbations are generally more apparent for low-energy electrons. The electron fluence simulations presented in this study illustrate the interplay between several factors that can make perturbation effects unpredictable in photon beams coupled to magnetic fields: (1) chamber and magnetic field orientation, (2) cavity size and shape, (3) extracameral components, (4) air gaps and their asymmetry, (5) electron energy, and (6) field size.

For reference fields, perturbations in electron fluence in ionization chambers due to the magnetic field are small or even negligible in some cases. However, for small fields, i.e.  $1 \times 1 \text{ cm}^2$ , the presence of a magnetic field leads to significant perturbations on electron fluence, especially in the low-energy region. Therefore, the determination of quality correction factors for small-cavity ionization chambers is crucial for small fields. Further investigations and corroboration of these factors from independent research groups are still needed.

The magnetic field strongly modifies the electron fluence in solid-state detectors for reference and small fields; hence they should be avoided in the clinic. Similarly, situations, where asymmetrical air gaps could occur, should be avoided, especially for the small-cavity chambers. The performance of detectors dedicated to dosimetry in the presence of a magnetic field can be improved by avoiding high-density materials surrounding the sensitive volume and non-uniform internal air layers.

# Acknowledgments

We gratefully acknowledge Ilias Billas and David Shipley for sharing the Monte Carlo model of the chamber PTW30013, and Jasmine Duchaine for the solid-state detector models. We also acknowledge PTW for providing the detectors blueprints and Elekta for sharing the Unity phases-spaces. We also acknowledge financial support by the Consejo Nacional de Ciencia y Tecnología (CONACyT) and the Natural Sciences and Engineering

Research Council of Canada (NSERC RGPIN/04178-2015). This research was enabled in part by the support provided by Calcul Québec (www.calculquebec.ca) and Compute Canada (www.computecanada.ca).

# Appendix A. Magnetic-field term in the radiation transport equation

The term due to the presence of the magnetic field in equation (2) can be developed as follows

$$q(\hat{\boldsymbol{u}} \times \boldsymbol{B}) \cdot \nabla_{p} f = q \nabla_{p} f \cdot (\hat{\boldsymbol{u}} \times \boldsymbol{B})$$

$$= q \boldsymbol{B} \cdot [\nabla_{p} f \times \hat{\boldsymbol{u}}]$$

$$= q \boldsymbol{B} \cdot \left[ \frac{1}{p} \left[ \frac{\partial f}{\partial \theta} \hat{\boldsymbol{\theta}} + \frac{1}{\sin \theta} \frac{\partial f}{\partial \phi} \hat{\boldsymbol{\phi}} \right] \times \hat{\boldsymbol{u}} \right]$$

$$= \frac{q}{p} \boldsymbol{B} \cdot \left[ \frac{\partial f}{\partial \theta} \hat{\boldsymbol{\theta}} \times \hat{\boldsymbol{u}} + \frac{1}{\sin \theta} \frac{\partial f}{\partial \phi} \hat{\boldsymbol{\phi}} \times \hat{\boldsymbol{u}} \right], \tag{A1}$$

choosing the coordinates such that  $\mathbf{B} = B\hat{\mathbf{z}}$  and recalling that the gyration radius is defined as  $R = \frac{p}{|q|B}$ . Then for electrons, q = -|q| and therefore

$$q(\hat{\boldsymbol{u}} \times \boldsymbol{B}) \cdot \nabla_{p} f = -\frac{1}{R} \hat{\boldsymbol{z}} \cdot \left[ \frac{\partial f}{\partial \theta} \hat{\boldsymbol{\theta}} \times \hat{\boldsymbol{u}} + \frac{1}{\sin \theta} \frac{\partial f}{\partial \phi} \hat{\boldsymbol{\phi}} \times \hat{\boldsymbol{u}} \right]$$

$$= -\frac{1}{R} \hat{\boldsymbol{z}} \cdot \left[ \frac{\partial f}{\partial \theta} [\sin \phi \hat{\boldsymbol{x}} - \cos \phi \hat{\boldsymbol{y}}] + \frac{1}{\sin \theta} \frac{\partial f}{\partial \phi} [\cos \theta \cos \phi \hat{\boldsymbol{x}} + \cos \theta \sin \phi \hat{\boldsymbol{y}} - \sin \theta \hat{\boldsymbol{z}}] \right]$$

$$= -\frac{1}{R} \hat{\boldsymbol{z}} \cdot \left[ \left( \sin \phi \frac{\partial f}{\partial \theta} + \cot \theta \cos \phi \frac{\partial f}{\partial \phi} \right) \hat{\boldsymbol{x}} + \left( -\cos \phi \frac{\partial f}{\partial \theta} + \cot \theta \sin \phi \frac{\partial f}{\partial \phi} \right) \hat{\boldsymbol{y}} + \left( -\frac{\partial f}{\partial \phi} \right) \hat{\boldsymbol{z}} \right]$$

$$= \frac{1}{R} \frac{\partial f}{\partial \phi}.$$
(A2)

# Appendix B. Radiation transport equation for the electron fluence spectrum

Considering a geometry in which the medium atomic properties are homogeneous, i.e. the first classical Fano condition is fulfilled, but with an arbitrary mass density distribution given by  $\rho = \rho(\mathbf{r})$  and defining a particle source as  $s_Q = s_Q(\mathbf{r}, \mathbf{p})$  and an homogeneous magnetic field  $\mathbf{B} = B\hat{\mathbf{z}}$ . The transport equation is given by

$$\hat{\boldsymbol{u}} \cdot \nabla_{r} f = \rho \left[ S_{Q} + \mathcal{I} \{ f \} - \frac{1}{R_{B\rho}} \frac{\partial f}{\partial \phi} \right], \tag{B1}$$

the solution of this equation is unique and defined by Q, B and  $\rho$ , noting the solution as  $f = f_{Q_B}^{\rho}$ . To integrate the transport equation of f over all directions, each term is integrated separately. First, the integration of the left term in equation (B1) is

$$\int_{4\pi} \hat{\boldsymbol{u}} \cdot \nabla_{r} f d\Omega = \int_{4\pi} \frac{\partial}{\partial x} [\sin \theta \cos \phi f(\boldsymbol{x}, \boldsymbol{p})] d\Omega + \int_{4\pi} \frac{\partial}{\partial y} [\sin \theta \sin \phi f(\boldsymbol{x}, \boldsymbol{p})] d\Omega + \int_{4\pi} \frac{\partial}{\partial z} [\cos \theta f(\boldsymbol{x}, \boldsymbol{p})] d\Omega$$

$$= \frac{\partial}{\partial x} \left[ \int_{4\pi} \sin \theta \cos \phi f(\boldsymbol{x}, \boldsymbol{p}) d\Omega \right] + \frac{\partial}{\partial y} \left[ \int_{4\pi} \sin \theta \sin \phi f(\boldsymbol{x}, \boldsymbol{p}) d\Omega \right] + \frac{\partial}{\partial z} \left[ \int_{4\pi} \cos \theta f(\boldsymbol{x}, \boldsymbol{p}) d\Omega \right]$$

$$= \frac{\partial}{\partial x} \left[ \frac{\int_{4\pi} \sin \theta \cos \phi f(\boldsymbol{x}, \boldsymbol{p}) d\Omega}{\int_{4\pi} f(\boldsymbol{x}, \boldsymbol{p}) d\Omega} F(\boldsymbol{x}, \boldsymbol{p}) \right] + \frac{\partial}{\partial y} \left[ \frac{\int_{4\pi} \sin \theta \sin \phi f(\boldsymbol{x}, \boldsymbol{p}) d\Omega}{\int_{4\pi} f(\boldsymbol{x}, \boldsymbol{p}) d\Omega} F(\boldsymbol{x}, \boldsymbol{p}) \right]$$

$$+ \frac{\partial}{\partial z} \left[ \frac{\int_{4\pi} \cos \theta f(\boldsymbol{x}, \boldsymbol{p}) d\Omega}{\int_{4\pi} f(\boldsymbol{x}, \boldsymbol{p}) d\Omega} F(\boldsymbol{x}, \boldsymbol{p}) \right]$$
(B2)

defining position-dependent and momentum-dependent functions

$$\langle \sin \theta \cos \phi \rangle_{Q_{B}}^{\rho} \equiv \langle \sin \theta \cos \phi \rangle_{Q_{B}}^{\rho}(\mathbf{x}, \mathbf{p}) = \frac{\int_{4\pi} \sin \theta \cos \phi f_{Q_{B}}^{\rho}(\mathbf{x}, \mathbf{p}) d\Omega}{\int_{4\pi} f_{Q_{B}}^{\rho}(\mathbf{x}, \mathbf{p}) d\Omega}$$

$$\langle \sin \theta \sin \phi \rangle_{Q_{B}}^{\rho} \equiv \langle \sin \theta \sin \phi \rangle_{Q_{B}}^{\rho}(\mathbf{x}, \mathbf{p}) = \frac{\int_{4\pi} \sin \theta \sin \phi f_{Q_{B}}^{\rho}(\mathbf{x}, \mathbf{p}) d\Omega}{\int_{4\pi} f_{Q_{B}}^{\rho}(\mathbf{x}, \mathbf{p}) d\Omega}$$

$$\langle \cos \theta \rangle_{Q_{B}}^{\rho} \equiv \langle \cos \theta \rangle_{Q_{B}}^{\rho}(\mathbf{x}, \mathbf{p}) = \frac{\int_{4\pi} \cos \theta f_{Q_{B}}^{\rho}(\mathbf{x}, \mathbf{p}) d\Omega}{\int_{4\pi} f_{Q_{B}}^{\rho}(\mathbf{x}, \mathbf{p}) d\Omega}$$
(B3)

 $\Rightarrow$ 

$$\int_{4\pi} \hat{\boldsymbol{u}} \cdot \nabla_{r} f_{Q_{B}}^{\rho} d\Omega = \frac{\partial}{\partial x} [\langle \sin \theta \cos \phi \rangle_{Q_{B}}^{\rho} F_{Q_{B}}^{\rho}(\boldsymbol{x}, p)] + \frac{\partial}{\partial y}$$

$$[\langle \sin \theta \sin \phi \rangle_{Q_{B}}^{\rho} F_{Q_{B}}^{\rho}(\boldsymbol{x}, p)] + \frac{\partial}{\partial z} [\langle \cos \theta \rangle_{Q_{B}}^{\rho} F_{Q_{B}}^{\rho}(\boldsymbol{x}, p)]$$
(B4)

note that  $f_{Q_B}^{\rho}$  as well as the functions in equation (B3) are entirely defined by Q, B and  $\rho$ . Thus, their explicit dependence on f can be omitted and be reported in terms of Q, B and  $\rho$ .

Defining the spectral source  $S_O$  as

$$S_Q \equiv \int_{4\pi} s_Q(\mathbf{x}, \mathbf{p}) d\Omega. \tag{B5}$$

Recalling that the interaction term is given by

$$\mathcal{I}{f(\mathbf{x}, \mathbf{p})} = -\Sigma(p)f(\mathbf{x}, \mathbf{p}) + \int_{p}^{\infty} dp' \int_{4\pi} f(\mathbf{x}, \mathbf{p}') \sigma(\mathbf{p}' \to \mathbf{p}) d\Omega'$$
(B6)

with the mass macroscopic cross section differential in momentum only defined as

$$\Sigma(p \to p') = \int_{4\pi} \sigma(\mathbf{p} \to \mathbf{p}') d\Omega'$$
 (B7)

and the mass macroscopic cross section defined as

$$\Sigma(p) = \int_0^p \Sigma(p \to p') dp'$$
 (B8)

then, the integration of the interaction term over all directions is

$$\int_{4\pi} \mathcal{I}\{f(\mathbf{x}, \mathbf{p})\} d\Omega = -\int_{4\pi} \Sigma(p) f(\mathbf{x}, \mathbf{p}) d\Omega + \int_{4\pi} d\Omega \int_{p}^{\infty} dp' \int_{4\pi} f(\mathbf{x}, \mathbf{p}') \sigma(\mathbf{p}' \to \mathbf{p}) d\Omega'$$

$$= -\Sigma(p) \int_{4\pi} f(\mathbf{x}, \mathbf{p}) d\Omega + \int_{p}^{\infty} dp' \int_{4\pi} f(\mathbf{x}, \mathbf{p}') \left[ \int_{4\pi} \sigma(\mathbf{p}' \to \mathbf{p}) d\Omega \right] d\Omega'$$

$$= -\Sigma(p) F(\mathbf{x}, p) + \int_{p}^{\infty} dp' \int_{4\pi} f(\mathbf{x}, \mathbf{p}') \Sigma(p' \to p) d\Omega'$$

$$= -\Sigma(p) F(\mathbf{x}, p) + \int_{p}^{\infty} \Sigma(p' \to p) \left[ \int_{4\pi} f(\mathbf{x}, \mathbf{p}') d\Omega' \right] dp'$$

$$= -\Sigma(p) F(\mathbf{x}, p) + \int_{p}^{\infty} \Sigma(p' \to p) F(\mathbf{x}, p') dp'$$

$$\equiv I\{F(\mathbf{x}, p)\}. \tag{B9}$$

Finally, the last term to integrate is

$$\int_{4\pi} \frac{1}{R_B \rho} \frac{\partial f}{\partial \phi} d\Omega = \frac{1}{R_B \rho} \int_0^{\pi} \sin \theta d\theta \int_0^{2\pi} \frac{\partial f}{\partial \phi} d\phi$$

$$= 0. \tag{B10}$$

From these results, the direction-integrated transport equation is

$$\frac{\partial}{\partial x} [\langle \sin \theta \cos \phi \rangle_{Q_B}^{\rho} F] + \frac{\partial}{\partial y} [\langle \sin \theta \sin \phi \rangle_{Q_B}^{\rho} F] + \frac{\partial}{\partial z} [\langle \cos \theta \rangle_{Q_B}^{\rho} F] = \rho [S_Q + I\{F\}]$$
 (B11)

with the solution expressed as  $F = F_{Q_B}^{\rho}(\mathbf{x}, p)$  being unique and entirely defined by Q, B and  $\rho$ .

#### **ORCID iDs**

Yunuen Cervantes https://orcid.org/0000-0002-8663-0673

#### References

Agnew J, O'Grady F, Young R, Duane S and Budgell G J 2017 Quantification of static magnetic field effects on radiotherapy ionization chambers *Phys. Med. Biol.* 62 1731–43

Billas I, Bouchard H, Oelfke U, Shipley D, Gouldstone C and Duane S 2020 Alanine dosimetry in strong magnetic fields: use as a transfer standard in mri-guided radiotherapy *Phys. Med. Biol.* 65 115001

Bouchard H and Bielajew A 2015 Lorentz force correction to the Boltzmann radiation transport equation and its implications for Monte Carlo algorithms *Phys. Med. Biol.* **60** 4963–71

Bouchard H, de Pooter J, Bielajew A and Duane S 2015 Reference dosimetry in the presence of magnetic fields: conditions to validate Monte Carlo simulations *Phys. Med. Biol.* **60** 6639–54

Cervantes Y, Billas I, Shipley D, Duane S and Bouchard H 2020 Small-cavity chamber dose response in megavoltage photon beams coupled to magnetic fields *Phys. Med. Biol.* 65 245008

Cervantes Y, Duchaine J, Billas I, Duane S and Bouchard H 2021 Monte carlo calculation of detector perturbation and quality correction factors in a 1.5 t magnetic resonance guided radiation therapy small photon beams *Phys. Med. Biol.* 66 225004

de Pooter J A, Billas I, de Prez L A, Duane S, Kapsch R P, Karger C, van Asselen B and Wolthaus J W H 2021 Reference dosimetry in mrilinacs: evaluation of available protocols and data to establish a code of practice *Phys. Med. Biol.* 66 05TR02

De Pooter J A, De Prez L A and Bouchard H 2015 Application of an adapted Fano cavity test for Monte Carlo simulations in the presence of B-fields *Phys. Med. Biol.* 60 9313–27

de Prez L, Woodings S, de Pooter J, van Asselen B, Wolthaus J, Jansen B and Raaymakers B 2019 Direct measurement of ion chamber correction factors, k q and k b, in a 7 mv mri-linac *Phys. Med. Biol.* 64 105025

Fano U 1954 Note on the bragg-gray cavity principle for measuring energy dissipation Radiat. Res. 1 237-40

Hackett S L, van Asselen B, Wolthaus J W H, Kok J G M, Woodings S J, Lagendijk J J W and Raaymakers B W 2016 Consequences of air around an ionization chamber: Are existing solid phantoms suitable for reference dosimetry on an MR-linac? Med. Phys. 43 39–61

Kawrakow I 2000 Accurate condensed history Monte Carlo simulation of electron transport: II. Application to ion chamber response simulations *Med. Phys.* 27 499–513

Kawrakow I, Rogers D W O, Mainegra-Hing E, Tessier F, Townson R W and Walters B R B 2000 EGSnrc toolkit for Monte Carlo simulation of ionizing radiation transport (https://doi.org/10.4224/40001303)

Malkov V N and Rogers D W O 2016 Charged particle transport in magnetic fields in EGSnrc Med. Phys. 43 4447-58

Malkov V N and Rogers D W O 2017 Sensitive volume effects on Monte Carlo calculated ion chamber response in magnetic fields *Med. Phys.*44 4854–8

Meijsing I, Raaymakers B W, Raaijmakers A J E, Kok J G M, Hogeweg L, Liu B and Lagendijk J J W 2009 Dosimetry for the MRI accelerator: the impact of a magnetic field on the response of a Farmer NE2571 ionization chamber *Phys. Med. Biol.* **54** 2993–3002

O'Brien D J, Roberts D A, Ibbott G S and Sawakuchi G O 2016 Reference dosimetry in magnetic fields: formalism and ionization chamber correction factors *Med. Phys.* 43 4915–27

O'Brien D J and Sawakuchi G O 2017 Monte Carlo study of the chamber-phantom air gap effect in a magnetic field *Med. Phys.* 44 3830–8 Pojtinger S, Kapsch R P, Dohm O S and Thorwarth D 2019 A finite element method for the determination of the relative response of ionization chambers in MR-linacs: simulation and experimental validation up to 1.5 T *Phys. Med. Biol.* 64 135011

Reynolds M, Fallone B G and Rathee S 2013 Dose response of selected ion chambers in applied homogeneous transverse and longitudinal magnetic fields *Med. Phys.* 40 042102

Scott A J D, Kumar S, Nahum A E and Fenwick J D 2012 Characterizing the influence of detector density on dosimeter response in non-equilibrium small photon fields *Phys. Med. Biol.* 57 4461–76

Shipley D, Billas I and Duane S 2019 Experimental benchmarking of monte carlo based detector response simulations in magnetic field 2nd Int. Conf. on Monte Carlo Techniques for Medical Applications (Montreal, Canada)

Spindeldreier C K, Schrenk O, Bakenecker I, Kawrakow A, Burigo L, Karger C P, Greilich S and Pfaffenberger A 2017 Radiation dosimetry in magnetic fields with Farmer-type ionization chambers: determination of magnetic field correction factors for different magnetic field strengths and field orientations *Phys. Med. Biol.* 62 6708–28

van Asselen B, Woodings S J, Hackett S L, van Soest T L, Kok J G M, Raaymakers B W and Wolthaus J W H 2018 A formalism for reference dosimetry in photon beams in the presence of a magnetic field *Phys. Med. Biol.* 63 125008

Wolthaus J, Van Asselen B, Woodings S, Van Soest T, Kok J, de Prez L, Jansen B, de Pooter J and Raaymakers B 2016 Th-cd-bra-03: Direct measurement of magnetic field correction factors, kqb, for application in future codes of practice for reference dosimetry *Med. Phys.* 43 3873–3873